Characterization and Computational Evaluation of a Genetically Encoded Fluorescent Probe for Reactive Oxygen Species

Yihan Wang

A thesis

submitted in partial fulfillment of the

requirements for the degree of

Master of Science in Bioengineering

University of Washington

2021

Committee:

Andre Berndt
Charles Chavkin
Amy Orsborn

Program Authorized to Offer Degree:
Bioengineering

University of Washington

Abstract

Characterization and Computational Evaluation of a Genetically Encoded Fluorescent Probe for Reactive Oxygen Species

Yihan Wang

Chair of the Supervisory Committee:
Professor Andre Berndt
Bioengineering

Reactive Oxygen Species (ROS) are highly reactive chemical molecules that have essential roles in physiological processes. H_2O_2 is a relatively stable member of ROS family in aqueous environment and serves as an important signaling molecule in various mechanisms, such as the opioid overdose and myocardial ischemia. Among the various analytical tools, genetically encoded fluorescent indicator (GEFI) is a profound technology that demonstrates high specificity and spatiotemporal resolution in capturing the physiological production of H_2O_2. We have developed HRM63, a H_2O_2 GEFI that demonstrates 2-times higher fluorescent magnitude and 10-times faster responding dynamic compared to HyPerRed, one of the most widely used H_2O_2 GEFI. For the scope of this thesis, my investigation includes the HRM63 sensor characterization, including its subcellular specificity, reversibility and photoactivation, and the overall computational pipeline of analyzing the fluorescent readout of HRM63. We develop a single-cell tracking algorithm Cell of Interest Nearest Neighbor (COINN) based on the result from Cellpose, a deep learning-based segmentation algorithm, to visualize the cell-to-cell difference in the fluorescent output of sensor-transfected cells. We then design a ratiometric sensor HRM63-mCherry to correct the effect of protein expression level. Combining the use of COINN and HRM63-mCherry, we present a new representation of fluorescent reading indicating the oxidation level that also accounts for the difference among individual cells. We also use the machine learning-based classification to predict whether the individual cells will respond to the agonist administration. Ultimately, these findings will allow more effective investigation on the pipeline of characterizing the H_2O_2 GEFIs using the fluorescent imaging.

TABLE OF CONTENTS

LIST OF FIGURES

LIST OF TABLES

ACKNOWLEDGMENTS

I would like to first and foremost like to thank my advisor, Dr. Andre Berndt, for giving me this opportunity to continue my undergraduate capstone project as a master student. It has been a honor for me to be under the mentorship of Andre, whose expertise is invaluable in formulating the research questions and guides me in every step of the way. I would like to especially thank my personal lab mentor, Justin Lee, for taking me as a mentee since my junior year in undergraduate and patiently supporting me throughout the journey of research, and for his dedication and passion in research that has influenced me for many years. I would like to thank all members from Berndt Lab for their help along my investigation: Netta Smith, Mike Rappleye, Jeanot Muster, Amanda Nguyen and Jamison Siebart. I also want to express my appreciation to Dr. Charles Chavkin and Dr. Amy Orsborn for being willing to participate in my supervisory committee and pointing me in the right direction whenever I needed guidance on my project.

Chapter 1

INTRODUCTION

The overarching purpose of this thesis is to investigate the research pipeline of detecting and quantifying the production of reactive oxygen species (ROS) in mammals. By characterizing a genetically encoded redox probe from the experimental aspects and exploring its performance in various *in cyto* circumstances, this thesis validates the potential of this probe to be applied in the disease-modeling studies involving ROS-producing mechanisms. Furthermore, this thesis also presents a cell tracking algorithm using nearest neighbor method to extract information from the *in cyto* fluorescent imaging and uses it to investigate the framework of quantifying the oxidative level from the fluorescent readout of the probe. The results of this thesis aim to facilitate the biomedical studies that require long-term ROS monitoring and provide insights towards the analysis of fluorescent images.

1.1 Background

1.1.1 Reactive Oxygen Species (ROS)

Reactive oxygen species (ROS) is a family of chemically reactive species produced in various enzymatic reactions that contain oxygen metabolism. Some examples of ROS include superoxide anion (O_2^-) and hydrogen peroxide (H_2O_2) [2]. All members of ROS family are highly reactive to the surrounding biological macromolecules due to their unstable molecular structure. ROS-generating processes have long and complex evolution in organisms. From the early cell-to-cell communication in unicellular organism to the complex regulation of growth, apoptosis and other cellular signaling in human, ROS have vital roles in many physiological processes [15, 16].

A delicate control over the intracellular ROS concentration is critical to maintain the redox balance in the organisms [15]. Multiple antioxidant processes are known to maintain the intracellular redox balance by catalyzing the ROS products into water and oxygen through the antioxidant enzymes, such as peroxiredoxins (PRX), glutathione peroxidases (GPX) and catalase (Figure. 1.1) [1, 17]. Overproduction of ROS can defeat the natural protection from the antioxidant enzymes and introduce oxidative stress to cells, causing a variety of DNA damage [16]. Because of its high reactivity, ROS can affect almost all DNA, proteins and lipids when it is in a pathophysiological concentration, especially the mitochondrial DNA that lacks the repair enzymes. Thus, ROS has been shown to relate to many age-associated diseases [15]. Recent research shows that pathophysiology of more than 200 types of diseases involves the production of ROS, such as cardiovascular lesion [16].

Compared to other short-living ROS molecules, H_2O_2 is relatively stable in aqueous environment and can last for several seconds. Thus, H_2O_2 can reversibly oxidize specific protein thiolates, serving as the host defense and oxidative inducer for many cell types [12]. The mounting evidence shows that low-level H_2O_2 also plays the role of an important signaling molecule in physiological condition [18]. Other reactive oxygen intermediates, such as O_2^-, undergo rapid dismutation to H_2O_2 upon production from enzymatic reactions [15]. The highly specific oxidation of thiolate groups by H_2O_2 enables the redox signaling involved the thiolate-containing proteins [2]. The antioxidant enzymes including catalase (Cat) and glutathione reduce the excessive H_2O_2 to water after H_2O_2 exits the mitochondria.

1.1.2 ROS in Opioid Misuse

Opioid has a long history of been used as an effective pain-relieving substance, but the risk of misuse and addiction of opioid introduce serious medical and societal problems regarding the drug overdoses [19]. Between 1999 and 2017, about 400,000 out of 700,000 deaths by drug overdose (56.8%) were related to opioids [20]. In 2016, an estimation of 2.4 million Americans has shown the misuse of opioid, including 0.6% of teenagers between 12 to 17 years old and 1.1% of adults between 18 to 25 years old. The cost of related medical care, such as ICU room admission, mechanical ventilation and vasopressor administration for opioid overdose also increased. The total estimated cost to society is about $504 billion, approximately 2.8% of the US gross domestic product (GDP) in 2015 [21].

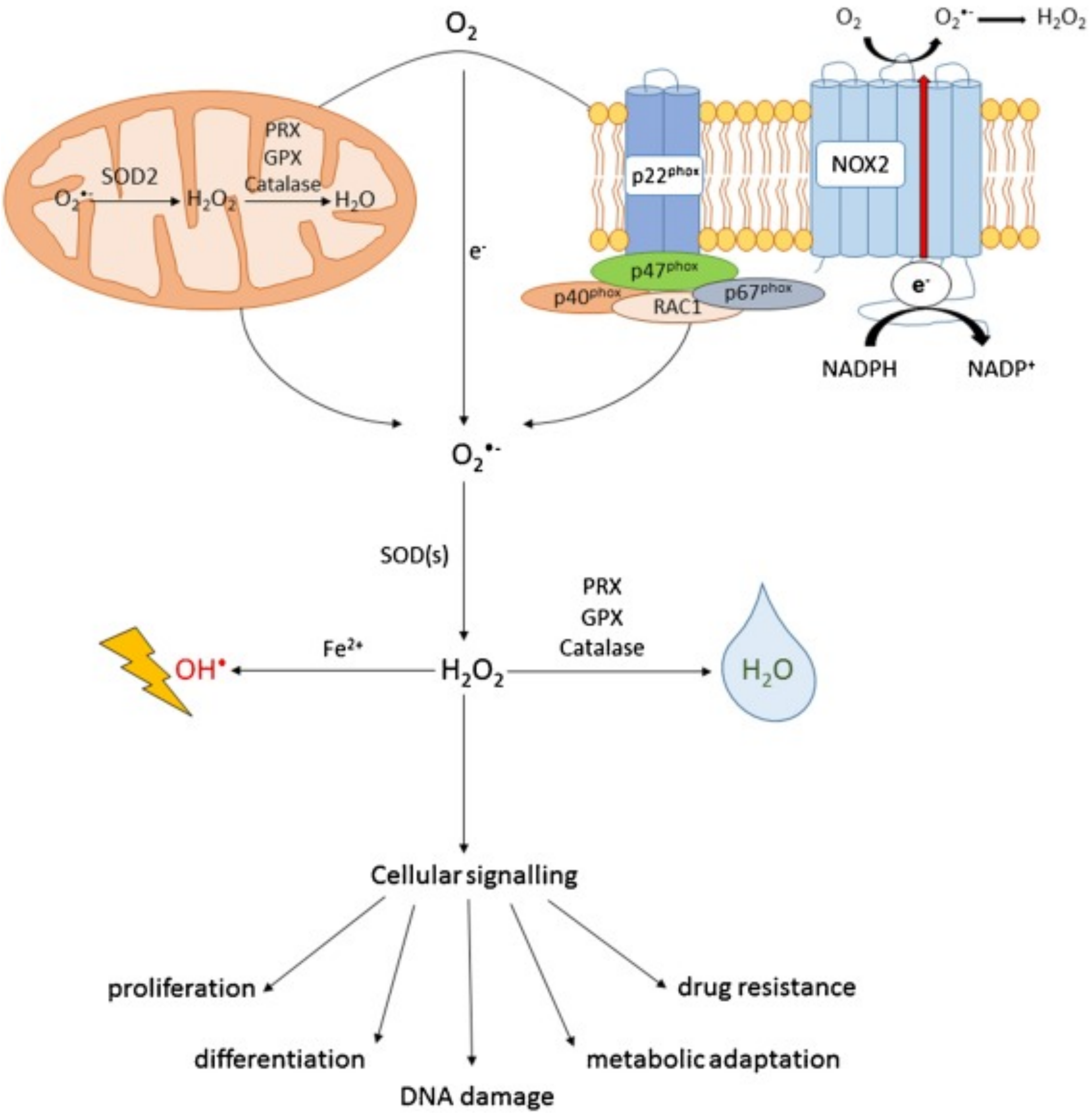

Figure 1.1: **Schematic showing of reactive oxygen species (ROS) production and regulation.** Through the oxygen-involved metabolic mechanisms, ROS are produced and delicatedly controlled by antioxidant enzymes, such as peroxiredoxins (PRX), glutathione peroxidases (GPX) and catalase. Hydrogen peroxide (H_2O_2) also serves as an important signaling messengers in many cellular mechanisms [1]

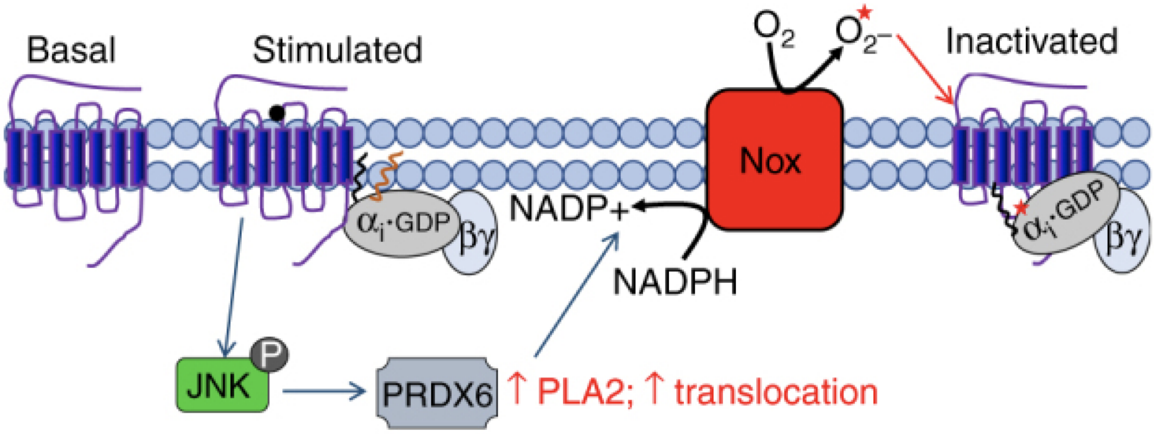

Figure 1.2: **Schematic showing of the role of ROS in regulating GPCRs in KOR inactivation.** ROS is generated through the NOX triggered by JNK-promoted PRDX6 localization. The generated ROS then inactivates the nearby GPCRs and lead to inactivation of KOR [2].

H_2O_2 serves as a signaling messenger in the neural mechanisms of opioid receptors reacting to opioid, a commonly prescribed pain relief used in anesthesia. Opioid receptor activation triggers analgesic mechanism by activating G- protein receptor kinase (GRK) but also causes the activation of a series of mitogen activated protein kinases (MAPK), such as c-Jun N-terminal kinase (JNK). It promotes the localization of peroxiredoxin 6 (PRDX6), triggering the production of H_2O_2 from the NADPH oxidase (NOX), which eventually leads to the reducing response of the kappa opioid receptors (KOR) (Figure. 1.2) [2]. Patients need to consume an increasing dosage of opioids to continue with the analgesic effects.

Inactivation of JNK is then crucial to the increase of opioid efficacy. Therefore, time-resolved measurements of H_2O_2 in intact neuronal circuits would be critical to fully dissect this signaling mechanism and contribute to the development of therapeutics for drug overdose and relapses.

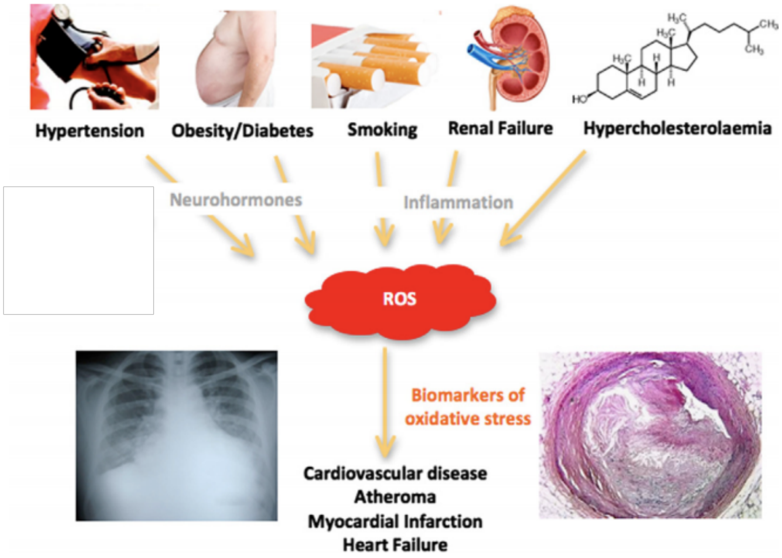

Figure 1.3: **Schematic showing of ROS in cardiovascular diseases.** ROS act as a mediator in many cardiovascular diseases. Thus, monitoring the production of ROS helps to integrate the relevent disease modeling [3].

1.1.3 ROS in Cardiovascular Disease

In order to maintain the continuous cardiac function, cardiomyocytes rely heavily on the mitochondrial metabolic reaction that produces O_2^- as a byproduct. The highly reactive O_2^- will rapidly go through the dismutation and become H_2O_2. Together with the endogenous production of carbon monoxide (CO) and nitric oxide (NO), H_2O_2 plays the role as a redox signaling molecule to induce antioxidant protection and cellular repair mechanism [3, 18].

However, when the endogenous ROS production exceeds the capacity of the local, the oxidative damage results in the changes in the expression of NOX 1, 2, 4 and 5, which are closely associated to the pathophysiological conditions of cardiomyocytes, such as ischemia/reperfusion (IR) or hypertension (Figure. 1.3) [15, 17, 18]. In a study using the *in vivo* human model to study the flow-mediated dilation of the endothelial IR injury, the result suggests that ROS produced by NOX are determinants of endothelial function after IR injury in human [22]. Genome study also reveals that a polymorphism in the promoter of the $p22^{phox}$ gene found in the spontaneously hypertensive rats lead to an overexpression of

NOX-1 subunit and a subsequent increase in ROS [23]. In the study of sarcoplasmic reticulum (SR) sarcolemma calcium uptake in cardiomyocyte, the oxidative stress can up-regulate the level of a sarcolemma membrane-targeted protein phosphatase, PP2Ce, which specifically regulate Phospholamban (PLN) that inhibits the Ca^{2+} uptake via SR calcium-ATPase 2a (SERCA2a), promoting ischemia reperfusion injury in the heart [24].

As the heart disease has been the leading cause of death of the world, its annual medical expenditures of $219 billion in the United States from 2014 to 2015 shows urgent need for proper diagnosis [25]. Developing the biosensors that quantify the ROS as the product of pathophysiological process is critical to understand the mechanism behind the cardiovascular diseases and can be further applied in the clinical practices.

1.1.4 Genetically Encoded Sensor

The technology of genetically encoded sensor, or genetically encoded Fluorescence Indicator (GEFI) enables the real-time monitoring of redox products in living cells [12]. Developed by fusing a fluorescent protein with another sensing protein that goes through conformational change upon binding of target molecules, GEFIs are capable of visualizing the chemical and biological dynamics of target molecules *in situ*.

The earlier generation of genetically encoded fluorescent protein ROS probes demonstrates the capability of this tool and provides valuable insights towards the intracellular production of ROS, but the low brightness and sensitivity of detecting ROS in low concentration limits their application [12]. Since the amount of ROS produced as the signaling messengers is usually at the basal levels, developing a ROS probe with high sensitivity, specificity and dynamic range is in urgent need.

Additionally, the application of ROS probe in various cell types needs to be validated in order to investigate the mechanism behind the tissue-specific production of ROS [17]. Mitochondrial H_2O_2 production decreases in cardiac tissues of sedentary rats with both exercise and high-fat, high sucrose diet, unlike in skeletal muscles where the same treatment leads to increased mitochondrial H_2O_2 production, due to different level of expression of thioredoxin-2 reductase in sedentary animals [26]. Thus, examining the redox-capacity in different cell types is important to characterize the sensor functionality.

1.2 Prior Work: Capstone

1.2.1 Overview

My undergraduate research capstone focused on the structure-guided engineering of the genetically encoded fluorescent protein probe for H_2O_2. We used the rational design of structure-guided engineering to alter the protein structure of the sensor, in order to increase its fluorescent output, expecting to improve the allosteric coupling between the H_2O_2 binding domain and the fluorescent reporter protein, as well as strengthening the network of hydrogen bonds surrounding the H_2O_2-binding residues.

Thus far, we had generated multiple sensor variants that demonstrate better fluorescent performance and faster response time to H_2O_2 stimulation compared to the existing H_2O_2 protein probes. The most recent variant HRM63 with a modified insertion site of the reporter domain exhibited at least 2-fold higher fluorescent output than of HyPerRed at $10\mu M$ H_2O_2 stimulation. Combined with its rapid responding time, this new variant had the potential to be applied to *in vivo* testing in ROS-induced signaling pathway research.

1.2.2 Results

Our developed sensor HRM63 was based on the scaffold of HyPerRed, a derivative from HyPer family which inserts a circularly permuted red fluorescent protein cpmApple onto the regulatory domain of OxyR (OxyR-RD), a bacterial protein dimer from *Escherichia coli* that selectively reacts to H_2O_2 via a single residue – Cys199. This residue embeds in a hydrophobic pocket that repels the charged reactive species, such as superoxide. Upon H_2O_2 stimulation, the thiolate deprotonation will expose Cys199 from the hydrophobic pocket and bring it closer to another cysteine residue Cys208, causing the formation of a disulfide bond (Figure. 1.4). Conformational energy induced by structural change of OxyR-RD leads to a change in spectral properties [11].

We first hypothesized that the green fluorescent protein tends to have a higher compatibility to the intracellular environment compared to the fluorescent proteins of other

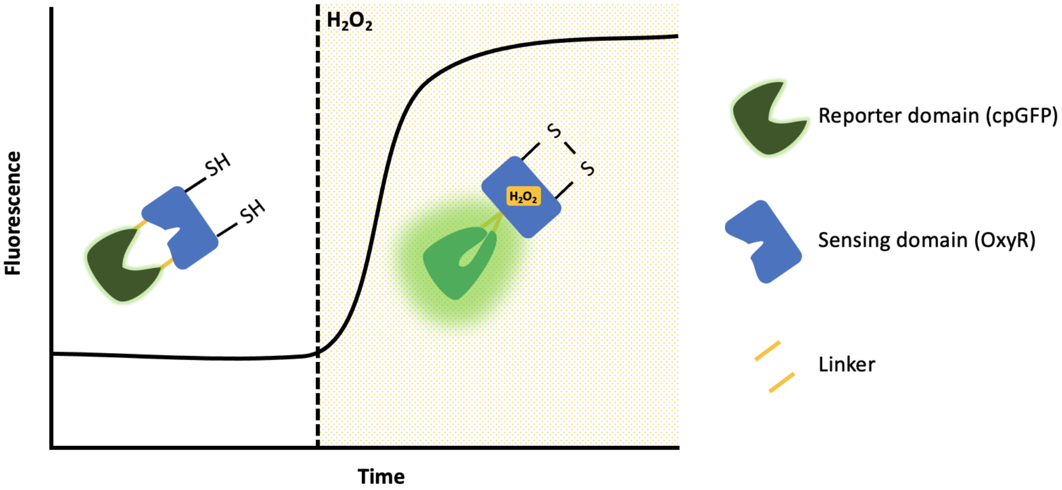

Figure 1.4: **Schematic showing of HRM63 and its response to H_2O_2.** H_2O_2 induces the formation of a disulfide bridge between two cysteine residues on the sensing domain, triggering the increases in fluorescence of the reporter domain.

wavelengths, demonstrating a higher fluorescent performance upon the stimulation. Thus, we replaced the cpmApple portion of HyPerRed with cpGFP from GCaMP6f [27] and cpsfGFP from ASAP2 [28]. The result showed a significant improvement in the fluorescent output upon $300\mu M$ H_2O_2 stimulation with both the reporter protein replacement and according linker optimization. We chose cpGFP to proceed based on its higher performance.

We then designed 8 variants named Hy43-50 with the new insertion site in the region of residues 210-215. The dynamic modeling of OxyR-RD protein indicated that while most of the OxyR-RD structure reminds unaffected by the binding of H_2O_2 molecules, the region between residues 205 to 225 exhibits the majority of conformational change due to the formation of disulfide bond between Cys199 and 208 [29]. We then hypothesized that the bulky fluorescent protein creates steric hinderance at the H_2O_2 reacting region and prevents the incoming H_2O_2 molecules from binding to the cystine residues. The new insertion site is still at the proximity with the disulfide bond region, retaining the conformational change that induces fluorescent output in the reporter region while avoiding the flexible loop

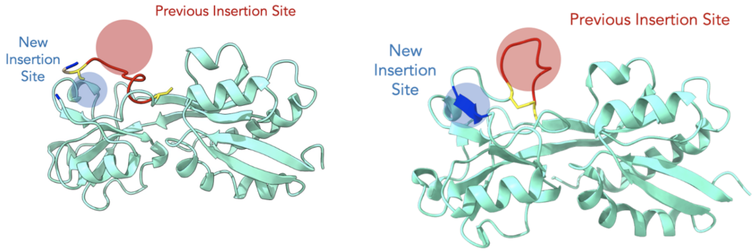

Figure 1.5: **3D view of the reductive and oxidative OxyR-RD with the binding site change.** New insertion site improves the fluorescent response and dynamic at low H_2O_2 concentration.

structure. We hypothesized that the new insertion site will optimize the spatial arrangement at the H_2O_2 binding site, which will improve the fluorescent performance (Figure. 1.5). Upon exposure to low concentration ($10\mu M$) of direct stimuli of H_2O_2, Hy44, 45, 46 and 47 demonstrated higher fluorescent output compared to HyPerRed under the wild-field microscopy.

We created the variants HRM60-75 based on the structure of Hy46 by introducing single mutation to the binding-site amino acid (residues 210-220). It is well documented that all GFP-like fluorescent proteins preserve a β-barrel structure outside the cavity containing the chromophores [30]. Hydrogen bonding between the chromophores and surrounding water molecules have significant effect on the fluorescent properties of protein [31]. The β-barrel structure also evolves to be less porous after chromophore formation, preventing the water molecules from interacting with the core [30]. Thus, we hypothesized that reducing water access to the core of cpGFP will improve its fluorescent performance (Figure. 1.6). The mutated amino acids were chosen to be large in size. Thus, we chose tyrosine proximal to opening of cpGFP. We expected that the large amino acids will block the opening on β-barrel structure of fluorescent protein, tightening the allosteric coupling and reducing the water access to the chromophores.

By screening the generated variants with the $300\mu M$ H_2O_2 stimulation, we recognized that the variant HRM63 demonstrates two-fold higher fluorescent output than Hy46 and all other constructs do (Figure. 1.7). This variant also exhibited a faster responding dynamic

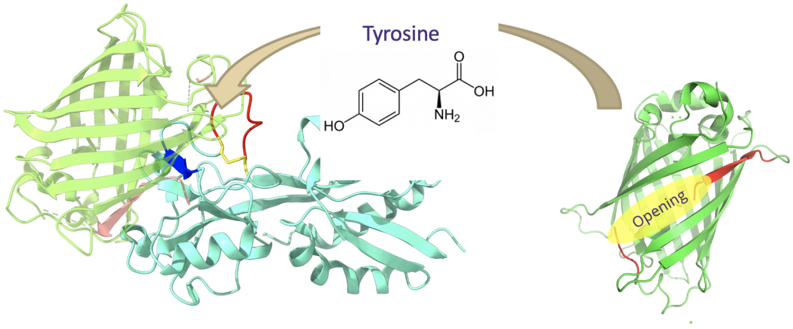

Figure 1.6: **3D representation of cpGFP inserted onto OxyR-RD at the new insertion site.** The opening of β-barrel structure will be genetically fused to the OxyR-RD at insertion site. Adding tyrosine to the insertion site reduces water access to the core of cpGFP, improving the fluorescent output.

compared to other variants, where the maximal fluorescent output was reached within the first five seconds. The outcompeting performance of HRM63 was also demonstrated at low H_2O_2 concentration. Fluorescent imaging of HEK293 cells expressing HyPerRed upon $10\mu M$ H_2O_2 stimulation showed very minimal fluorescent change that was not distinguishable by human eyes, while HRM63 displayed obvious increase in its fluorescent output with the same H_2O_2 concentration. Both sensors exhibited noticeable fluorescent change with the saturation H_2O_2 stimulation. Thus, for further experiments, we selected HRM63 as our final product.

1.3 Scope of Thesis

My research after finishing the capstone has been characterizing the developed HRM63 sensor, including testifying its chemical properties and validating its functionality in various types of cells. Using a series of characterization experiments, we confirm the subcellular sensitivity, specific photo-activation and reversibility of HRM63. We also develop a ratiometric sensor by fusing a red and constitutitively fluorescent protein named mCherry with HRM63. This ratiometric variant normalizes the green fluorescent readout of HRM63, serving as an attempt to quantify the oxidation level of the sensor-encoded cells by reducing the biological artifact during the imaging process.

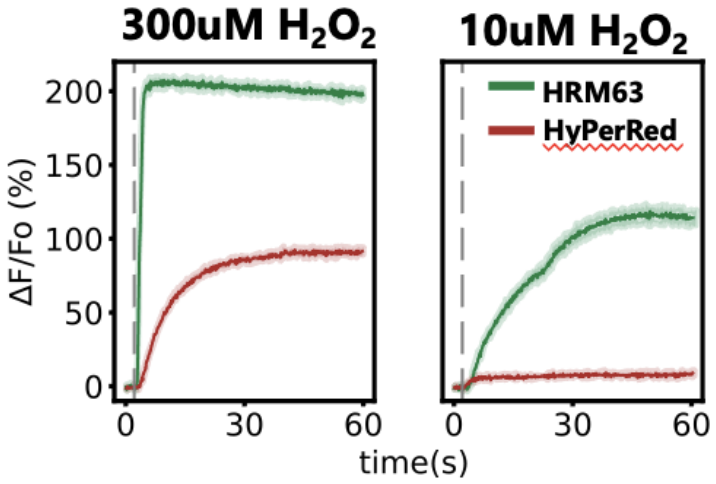

Figure 1.7: **Performance of HRM63 with saturation- and basal-level stimulation of H_2O_2 compared to HyPerRed.** HRM63 demonstrates almost 2-fold fluorescent change upon saturation-level H_2O_2 administration ($300\mu M$) and also exhibits obvious change with basal level of H_2O_2 stimulation ($10\mu M$). The performance of HRM63 in both scenarios exceeds that of HyPerRed.

A parallel portion of my research is on exploring the computational pipeline of extracting information from the fluorescent imaging. We develop a Python script that uses the nearest-neighbor method to maintain the ROI identities across the frames, visualizing the single-cell variance in the time-lapse fluorescent imaging of H_2O_2 sensor. Using this algorithm, we are able to investigate how the biological variance, such as cell size, location and shape, affects the fluorescent readout of the sensor-transfected cells. Combining with the ratiometric design, it aims to provide a more trustworthy analysis of the fluorescent output, facilitating the use of our developed sensor in oxidation level quantification.

Chapter 2

LITERATURE REVIEW

This section aims to provide an overview of the current literature that share the same interest as in this thesis. Continuing from the brief background on GEFI provided in the previous section, this section explores the genetically encoded H_2O_2 probe into more depth, identifying the pros and cons of the current technologies. Since the prevalence of COVID19, the focus of this thesis has been shifted to the computational analysis of the acquired data. Thus, it is necessary to analyze this field that was relatively new to our research, including the current cell tracking and segmentation algorithms used in image analysis, in order to improve our current approach of computational data analysis and to acquire more accurate information from the fluorescent readout in the experiments.

This section introduces the theoretical background for understanding the methods and motivation for the algorithms and analysis that will be described in the later chapters.

2.1 Genetically Encoded H_2O_2 Sensor

2.1.1 Overview

The discovery of ROS in the opioid-receptor signaling and cardiovascular disease modeling described in the previous section only represents a tiny portion of the existing researches involving ROS. However, the analytical process in this area of research is hindered by the unstable nature of ROS molecules. The traditional analytical processes are either unable to capture the transient presence of ROS or failing to ensure the purity of the molecules before they go through oxidation [32]. Though some biomarkers demonstrate great potential in clinical use [33, 34] or are able to measure the ROS in gene-expression level [35], but either the lack of selectivity or the labor-intensive imaging process limits their application [3, 32]. There are also fluorescent dyes that have low molecular weight and demonstrate optical change upon stimulation, but their invasive dye-loading process can change the metabolism and thus alter the redox readout.

Benefited from its ability to deal with the highly reactive molecules in real time, GEFI represents a revolutionary technology in understanding the redox nature [32]. GEFIs provide multiple advantages compared to other biomarkers in detecting ROS:

1. GEFIs can be designed to target the subcellular compartments, which enables the detection of ROS in the matrix [36] and mitochondria [37].

2. GEFIs are highly specific towards the targeted molecules because of its protein dynamic constraints. For example, the sensing domain of HyPerRed prevents the access of O_2^-, retaining its specificity towards H_2O_2 [11].

3. GEFIs are benefited from the ultra-fast dynamic of protein, having a responding time in millisecond scale that is able to capture the transient production of ROS.

4. The sequence of GEFIs can be modified to target only a subpopulation of the cells, such as the muscle cells [36] or neurons [38].

5. GEFIs are reversible [12, 32], enabling the long-term monitoring of the relevant mechanism and reducing the labors of repetitive loading.

6. GEFIs can be used in transgeneic organisms, ensuring the reproducibility of the testing results [32].

All these advantages contribute to a rising research interest towards the genetically encoded ROS sensors. There exists numerous types of functional redox GEFIs use different parameters to reflect redox status. For example, roGFP1, one of the most widely spread sensors that couples the redox-active cysteine residues to the β-barrel surface of GFP in spatial proximity to its chromophore, uses the glutathione redox potential E_{GSH} to measure the redox status [32, 39]. There are also sensors like Peredox that detects NADH/NAD+ registration using the bacterial repressor protein Rex [40]. In the scope of this thesis, only the GEFIs that specifically target H_2O_2 will be accessed. More specifically, the two H_2O_2-detecting families of widely used H_2O_2 probes, HyPer and roGFP-coupled probes, will be introduced to details and summarized as in Table A.1. Other H_2O_2 GEFIs, such as TriPer [41], also demonstrate great functionality, but will not be included in this thesis.

2.1.2 HyPer Family

The HyPer family refers to a group of H_2O_2-detecting biosensors [8, 9, 10, 11, 12]. The design of the first member named HyPer was reported in 2004 by Belousov *et al.*, consisting of the regulatory domain of a H_2O_2-sensitive transcriptional factor OxyR (OxyR-RD) from *Escherichia coli* and the sensing domain of cpYFP inserted into the flexible region between the residues 205–225. This design serves as a pioneer in the H_2O_2-detecting GEFIs, as it first uses the OxyR-RD as the sensing domain, which grants the sensor high H_2O_2 specificity. The key to the H_2O_2 sensitivity is the residue pair of Cys199 and Cys208, where Cys199 is released from a hydrophobic pocket once it is oxidized by H_2O_2 and forms a disulfide bridge with Cys208 [8]. The hydrophobic pocket also prevents the access of other ROS radicals like O_2^- [29]. The conformational change induced by the binding of H_2O_2 alters the biochemical environment surrounding the reporter domain, causing an intensity change of the chromophore. HyPer demonstrates its performance *in cyto* in the experiments with growth factor stimulation in HeLa cells, but the authors also identify the problems of its inability to detect low concentration of H_2O_2.

The second and third generation of this sensor, HyPer-2 [9] and HyPer-3 [10], retain the same protein structure as in HyPer but the newly introduced mutation improves the performance at low-H_2O_2 concentration and expands the dynamic range of the sensor [9, 10, 32]. HyPer-3 also demonstrates the *in vivo* performance of this sensor in zebrafish larva [10].

The later variant of HyPerRed replaces the reporter domain in the previous three generation with cpmApple and serves as an intensiometric sensor with one excitation and one emission wavelength [11]. This new variant, which is also the scaffold of our developed sensor, reduces the labor of working with ratiometric sensors that have multiple excitation wavelengths and shows improved sensitivity at low H_2O_2 concentration. HyPerRed is also the first redox sensor that uses the red spectrum, enabling its co-application with multiple messengers and synthetic dyes [11].

HyPer-7, the newest generation of HyPer family, is reported by Pak *et al.* recently. Its sensing domain is replaced by the OxyR-RD from another strain of bacteria named *Neisseria meningitidis*. They also introduce multiple mutations to the reporter domain of cpGFP that greatly increases the brightness [12]. HyPer-7 demonstrates much enhanced brightness and sensitivity compared to its predecessors, and its pH-stable property also add on to its application *in vivo* [32]. It also provides great insights to our future sensor design in terms of elevating the brightness and retaining the pH stability of the sensor upon redox status changes.

2.1.3 roGFP Family

The name "roGFP" stands for "reduction-oxidation-sensitive GFP". The first roGFP sensor described in the overview section was designed in 2004 by Hanson *et al.* [39], but its target of glutathione peroxidases are highly reactive with H_2O_2 [42]. Since H_2O_2 itself acts as an important signaling messenger in many mechanisms [2], sensor specificity towards H_2O_2 is necessary to provide valid measurement.

Thus, two H_2O_2-specific roGFP-coupled sensors, roGFP2-Orp1 [13] and roGFP2-Tsa2ΔC_R [14], are designed by fusing Orp1 or Tsa2 peroxiredoxin to roGFP2, respectively. Both structures utilizes the mechanism of oxidative redox relay, which is the intrinsic property of peroxiredoxin to promote oxidation of other protein in a proximity-dependent manner [13, 14]. Orp1 naturally mediates the oxidation of a transcription factor Yap1 by forming a sulfenic acid (Cys-SOH) at Cys36 that reacts with the thiol Cys598 of Yap1. Gutscher *et al.* shows that the oxidation-mediation of Orp1 is not restricted to Yap1, which can be used to create a H_2O_2-specific sensor combined with roGFP2 [13]. Morgan *et al.* improves the kinetic dynamic of this sensor by replacing the Orp1 with Tsa2, a mammalian 2-Cys peroxiredoxin that reacts to H_2O_2 binding 100-times faster than the sensing domain of HyPer and roGFP2-Orp1 [14]. Both sensors demonstrate functionality in H_2O_2-specific detection, and roGFP2-Tsa2ΔC_R also achieves basal-level H_2O_2 detection and subcellular compartment specificity [13, 14].

In terms of our sensor design, though we choose HyPerRed as the scaffold of our developed sensor, the studies on roGFP2-Orp1 and roGFP2-Tsa2ΔC_R reveal important chemical nature behind the H_2O_2-specific oxidation processes in proteins. For example, Gutscher *et al.* explains to detail that the peroxidases act as the catalyses to accept the H_2O_2 and convert the oxidation to a target protein, overcoming the activation barrier and ensuring the H_2O_2 specificity [13]. It provides new insights towards the mechanisms of H_2O_2-triggered proteins, facilitating our future design on improving the H_2O_2 specificity and sensitivity of our sensor.

2.2 Computational Analysis of Fluorescence Image in H_2O_2 Sensors

2.2.1 Overview

The ultimate goal of using our developed H_2O_2 sensor is to reveal the redox status in the targeted cells or tissue. However, there has not yet been a clear standard of evaluating the performance of H_2O_2 probes. The fluorescent readout of the intensiometric sensor HyPerRed is normalized to the baseline where zero stimuli is applied [11, 12]. The equation is as shown below:

$$\frac{\Delta F}{F_0} = \frac{F - F_0}{F_0}, \tag{2.1}$$

where F_0 represents the average intensity of the frames where zero stimuli is applied and F is the average intensity of the current frame. Most of the ratiometric H_2O_2 biosensors introduced above characterize their performance of the sensor by the ratio of dividing the intensity of the emission signals excited by different wavelengths [8, 9, 10, 12, 13]. In the study of roGFP2-Tsa2ΔC_R, Morgan *et al.* uses an equation to describe the degree of sensor oxidation (OxD) as shown below:

$$OxDroGFP2 = \frac{I405_{sample} * I488_{red} - I405_{red} * I488_{sample}}{I405_{sample} * I488_{red} - I405_{sample} * I488_{ox} + I405_{ox} * -I405_{red} * I488_{sample}}, \tag{2.2}$$

where I represents the acquired fluorescent intensity at emission wavelength 510nm after the excitation with either 405nm or 488nm wavelength. The subscription of 'ox' and 'red' represent the fluorescent output of the fully oxidized and fully reduced control, and 'sample' represents the sample fluorescent intensity [14]. This method takes the expression level of protein sensors into consideration, providing a more convincing evaluation of the sensor performance. However, none of the studies mentioned above reckon with the cell diversity in the image processing and analysis, where the fluorescent output is usually taken by the average of all cells present in a single frame.

Indeed, several studies published in the recent decades have shown that cells from the same population have heterogeneous protein expression, resulting in a wide range of cellular activity and differing abilities to adapt to changing environments [43, 44, 45]. A study reported by Radzinski *et al.* uses a flow cytometry-based methodology to investigate the individual differences in redox status in yeast cells coupled with roGFP2-Grx1 and shows that the ratio between the oxidized and reduced cells increases during aging [44]. This result confirms the effect of cell-to-cell variability in reflecting oxidation level. However, the complex experimental procedures of methodology based on flow cytometry may not be suitable for GEFI development, as the variant screening and characterization usually requires a large number of testing. A labor-free methodology of examining the individual difference in oxidation level in response to stimuli is necessary to the development and application of H_2O_2 sensors.

Moreover, in the studies of HyPer sensors that were reported between 2006 and 2015, the image processing of time-series data after recording the fluorescent output from the microscopes is mostly summarized as using the software of ImageJ [8, 9, 10, 11, 46]. However, in the recently published study of HyPer-7, Pak *et al.* additionally perform the background subtraction in each wavelength by taking a specified region of background for each experiment and subtracting it by every pixel using Microsoft Excel [12]. It shows a growing interest in optimizing the image processing and analysis paradigm to extract more useful information from the time-series fluorescent data of cells transfected with H_2O_2 sensors.

Image processing and analysis refer to two distinct but intersecting fields, where image processing as a branch of signal processing aims to improve the quality of the acquired images and image analysis investigates on how to extract the most valuable information from the images [47]. The combination of these two techniques should contribute to improve the performance evaluation of H_2O_2 sensor. One thing to note is that the image analysis paradigm in bio-imaging usually require both the methods of interpreting the images and the prior knowledge of the relevant biology as inputs. Thus, this section aims to investigate the fields in computational analysis of fluorescent images, including cell segmentation, tracking and classification, that are specifically related to the analysis of fluorescent H_2O_2 sensor.

2.2.2 Cell Segmentation

Image segmentation is usually the first step in image analysis, referring to delineating the regions of interest (ROIs) [47]. This process has a long history in bio-imaging analysis, because tracking the quantitative information of individual cells over the course of a time-lapse experiment is always necessary to interpret the cellular behavior [48]. Because the initial stage of our sensor development is composed of all *in cyto* experiment, this thesis only analyzes the segmentation of cells. The word "ROI" and "cell" will be used interchangably to represent the target of segmentation in the following sections. The current cell segmentation algorithms can be classified into two categories :

1. Contour-based segmentation, which first detects the edges of ROIs and then fills the target region;

2. Region-based segmentation, which starts with a seed region and grows until a significantly deviate image region is reached [49].

More subdivisions regarding the cell segmentation algorithms can be based on image features that are computed to determine the segmentation, such as local intensities, ROI shape or cell textures [48]. Manual-labeling and thresholding methods represent the primary versions of contour-based and region-based segmentation methods, respectively. Both methods were used in the image data analysis during the variant screening of our sensor development. However, the delineating accuracy of these two methods is not desirable. Since the fluorescent images are considered to have low signal-to-noise ratio (SNR) due to the

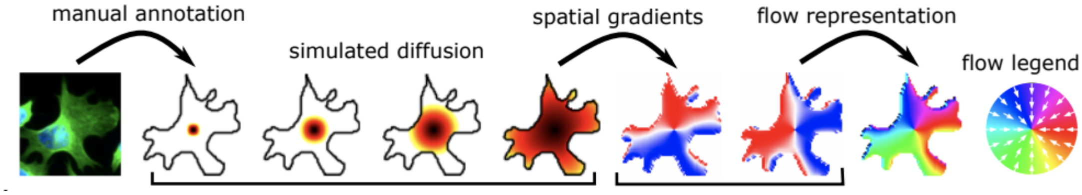

Figure 2.1: **Pre-neural-network processing of the training data in Cellpose.** The simulated diffusion is used to transform the manual labelling of boundaries to vector flow representation [4].

diffraction artifacts [47], choosing an optimized threshold that perfectly separates the cells and background is almost impossible (Fig A.1). An advanced region-based segmentation method is the watershed transformation [50, 51, 52]. It uses the intensity gradient and treats the images for analysis as a topographic map where the pixel value represents the height of the "drainage basin" and line going through the ridge is defined as the border. This method improves the accuracy of segmenting the attached cells, but it has problems with the overlapping cells [4]. In the case of manual labeling, the analysis efficiency is very low if the total number of cells exceed 10 at each frame. With the aid of image analysis software, such as ImageJ [46], the separation result is improved but still fails to resolve some of the problems, such as touching cells or unbalanced fluorescent protein expression in cells. Moreover, the problem with many current algorithms is the lack of generality [47]. Cells of different kinds have various shapes and characteristics, causing the image segmentation method to follow the case-by-case approach. Because we need to characterize our sensors in various cell types, using a generalist algorithm to standardize the segmentation results collected from different types of cells is preferred.

A recently published generalist algorithm for cellular segmentation named Cellpose becomes a suitable fit for our segmentation need. Based on the topological representation from watershed transformation, Cellpose generates a vector flow representation from the manual annotation of mask, where the flow starts at the center of the ROI and creates a spatial gradient towards the center (Figure. 2.1). This process is named as simulated diffusion. A neural network is then trained using the generated flow to predict the horizontal

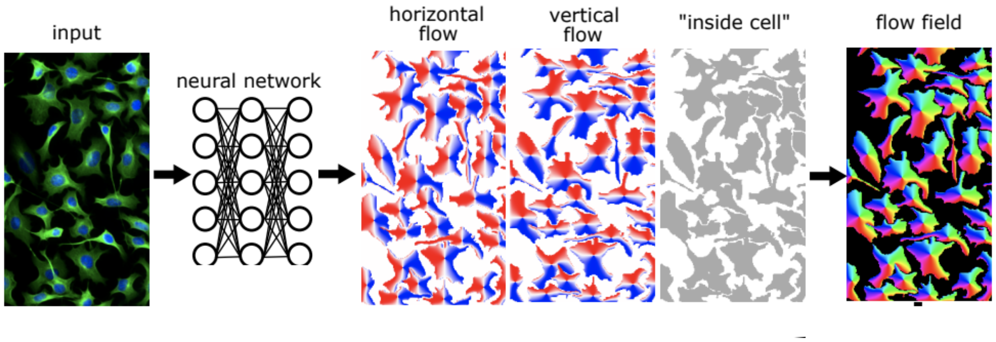

Figure 2.2: **Schematic showing of neural network processing in Cellpose.** Neural network is trained to predict the horizontal and vertical flows and possibility map to compute the flow field for cell segmentation [4].

and vertical flows and the possibility map determining if a pixel is within the region of a cell (Figure. 2.2) [4]. The architecture that this neural network is based on is the u-net convolutional network architecture, which was the algorithm that achieved the best score in the most difficult transmitted light microscopy categories in Cell Tracking Challenge at ISBI in 2015 [4, 53]. More importantly, Cellpose as a fast generalist algorithm trains the neural network on a dataset of highly varied images of cells and still outperforms many of the models trained on the specialist data [4]. It enables Cellpose to be used in variant screening and characterization in H_2O_2 sensor design for reproducible results.

2.2.3 Cell Tracking

In the studies of many genetically encoded H_2O_2 sensors, single-cell cell tracking is not a necessary process in the image analysis, because the intensity values are represented by the average intensity of all ROIs in each frame, where the temporal correspondence of the single cell is neglected. However, the importance of cell-to-cell difference has been stated in many other biological studies [43, 44, 45], indicating the need of single-cell tracking in time-lapsed imaging. Cell tracking represents the method of following an object over the course of a time-lapse experiment [47, 48]. The traditional cell tracking is usually done by manual labeling, which is labor-intensive and also error-prone [54]. Thus, using a computational software to track cells does not only improve the efficiency and accuracy, but also ensures the reproducibility of the result. The current tracking algorithms can be classified [48] into two groups:

1. Tracking by model evolution, where segmentation and tracking are performed simultaneously for the first frame and the derived model evolves in every consecutive frame [48, 54, 55, 56];

2. Tracking by detection, which first segments the cells in all frames and then identifies the temporal correspondence between the segmented cells from frame to frame [48, 57]

One of the most widely used model-based method is the active contour approach [54, 55, 56]. In this method, the process of segmentation and tracking is described as a model, where both the image-dependent and image-independent data contribute to the evolution of the model. The segmentation of the first frame is used to initialize the segmentation of the second frame [54, 56]. The cells can be represented as the closed contours or intact surfaces. The evolution equation is usually defined by the energy minimization, where the minimal energy is at the boundary. One advantage of this type of tracking is that the computational results from all previous frames, or *a priori* knowledge, are used to compute the model of the sequential frames [54], assisting the separation of the touching cells [56]. Though this approach was used in many recent studies of computational cell segmentation and tracking [58, 59, 60], its complexity to implement is not desirable for the purpose of our research. The advantages of model-based method include its precision in detecting the cell events, such as the cell division, but it is not a problem to consider in the experiments of sensor design and validation. Additionally, Cellpose as a generalist method serves as a simple and suitable tool for 2-D fluorescent image analysis in the sensor characterization of HRM63. As we also need image analysis on the 2-D image, a computationally simple detection-based method for single-cell tracking that incorporates with Cellpose segmentation is then a better choice for our research.

The first step of the detection-based cell tracking methods is to choose the appropriate image features in the segmented images that describe the position and identity of the cells in each frame. The simplest method is to find the centroids of the detected cells [49, 61]. In a study of detection-based tracking, Al-Kofahi *et al.* designs a feature vector that represents each cell in each frame using six image features, including centroids (both x- and y- positions), area, eccentricity, major axis length and orientation [62]. The simplest linking strategy of cells in different frames is the nearest-neighbor assignment, where the cells in the current frame are linked to the closest cells in the next frame [49]. This approach is possible for the fluorescent imaging if the ratio between the cell displacement across the frame and the mean distance between cells in a single frame is $<<0.5$ [63]. Thus, this method is suitable for tracking cells that lack motility under wide-field microscope. Choosing a comparatively simple tracking method also compensates the long processing time of Cellpose segmentation due to high computational complexity. One challenge for such detection-based tracking is to resolve the one-to-many and many-to-one correspondence in the consecutive frames [49, 56]. In the analysis of fluorescent images regarding H_2O_2 sensor characterization, we assume no occurrence of cell division during the course of imaging, but the detached cells that leave the field of observation or the cells that are not detected by Cellpose in segmentation are the factors we consider during analysis. Additionally, Cellpose is not a perfect segmentation method. It occasionally fails to detect some cells that have been identified in the previous frame. Thus, the Cellpose-based tracking method needs to take these problems into consideration.

2.2.4 Cell Classification

After the accurate single-cell segmentation and tracking, how to properly use the extracted image properties becomes the next topic. The complex heterogeneous phenotypes demonstrated by cells have made the interpretation of the cell response to stimulation a difficult task [44, 45]. In the past, we have made many attempts to reduce the trail-to-trail variance, such as maintaining the position of needle to administrate the agonist at the center of the cell culturing well. With the single-cell tracking, we will also be able to analyze the heterogeneity among the individual cells. A common approach to perform such analysis is to separate the cells into two or more categories, which is also know as cell classification.

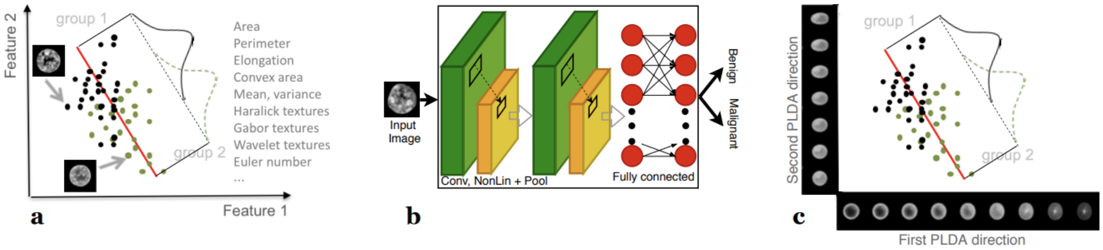

Figure 2.3: **Schematic showing of three different categories of cell classification.** **a.** Numerical feature extraction (NFE). **b.** Neural network (NN). **c.** Transport-based morphometry (TBM).

Shifat-E-Rabbi *et al.* summarizes the cell classification approaches into three categories (Figure.2.3):

1. Numerical feature extraction (NFE), which collects the pre-determined features from the segmented cells and uses them to classify the cells with a classifier;
2. Neural network (NN), which learns the features from the raw data by itself and uses these extracted features to classify;
3. Transport-based morphometry (TBM), which transforms image into a non-linear representation that shows the interpretable differences between classes [45].

Because we will perform the single-cell segmentation and tracking before the classification, the numerical feature-based cell pattern classification methods best suit our need. Indeed, this approach has been used to detect the functionality of subcellular proteins [64, 65]. Many features, such as area, perimeter, elongation and variance, have been tested to discriminate the cells, but the importance of features varies across datasets [45]. The six image features proposed by Al-Kofahi *et al.* for cell detection can serve as a start for cell classification.

Chapter 3

METHOD

This section introduces the experimental procedures and computational processes used to generate the results described later in this thesis. The experimental procedures are the *in cyto* testing of GEFIs, including the variant generation, cell culture, DNA transfection, stimulation-induced fluorescent imaging. The computational processes focus on the image processing and analysis of the acquired fluorescent images, including background subtraction, cell segmentation, single-cell tracking and classification.

3.1 Library Generation and DNA Cloning

Protein structure modifying prediction was achieved through Chimera and GENtle. Primers were designed using NEB Builder Assembly Tool website. Q5 High-Fidelity DNA Polymerase was used for PCR amplification. Backbone and insert DNA fragments varied according to the desired outcome from the sensor. Hy46 had the backbone DNA as the OxyR-RD DNA extracted from HyPerRed [11] and inserted the GcaMP6f [27] at a designated location within the region of residues 210-215. HRM63 was designed using the structure of Hy46 as the backbone and inserted GCaMP6f onto a new insertion site as described in the prior work. HRM63-mCherry ratiometric variant was designed by fusing a mCherry to the non-flexible region of the OxyR-RD. Visualization of the DNA fragments was achieved in agarose gel electrophoresis using SYBR Safe. PCR purification and spectrophotometer check were used on the DNA fragments prior to the DNA cloning using Gibson Assembly. Bacterial transformation of the full-length DNA product used Top 10 competent cells plated with 50 μL Super Optimal Broth (SOB) on a petri dish. Three individual colonies from each dish of variant were picked and cultured. DNA isolated from the bacterial colonies after 15-hour growth were purified and sent to GeneWiz for sequencing. One colony of each variant was selected based on its genetic similarity to the planning sequence.

3.2 Cell Culturing and Transfection

Human embryonic kidney (HEK293) cells were seeded at a density of $5*10^5$ cells/well in 24-well cell culturing plates after they reach 70% confluency. Cells were cultured in Dulbecco's modified eagle medium (DMEM) with 10% fetal calf serum (FCS) in the incubator with 37 °C and 5% CO2 for 24 hours. Transfection using 1.5 ug Lipofectamine 3000 reagent, 2 μL P3000 reagent, 100 μL Opti-MEM medium and 1 ng DNA for each construct was performed when the confluency of cells reached 70% - 90%. After 6 hours, media of the cells was replaced with fresh DMEM and cells were put back to incubator for at least 24 hours before imaging.

The cardiomyocytes derived from human-induced pluripotent stem cell (hiPSC) were offered by Dr. David Mack and his research group. The differentiation procedures were documented in the recently published study by Klima *et al.* [66].

3.3 Fluorescent Imaging and H_2O_2 Stimulation

Media of cells was replaced with 600 μM of Living Cell Imaging Solution (LCIS), a clear cell media that reduced the noise of spectrum absorption from phenol red. Cells were placed into the incubator for 5 minutes after media change. Microscopy Leica DMI8 was used to capture the fluorescent feedback from the cells.

MetaMorph, an imaging analysis software, was used to record the live imaging of cells upon stimulation [67]. Imaging was taken with an exposure time of 100 ms. Light intensity was set to 40 units and can be varied between 20 to 80 units according to the baseline fluorescent value. For HRM63, the band-pass excitation wavelength of 450-490 nm was set and the emission of 500-550 nm was captured. For HRM63-mCherry variant, each well was imaged for twice, where the first shot used the filter of HRM63 and the second shot used an excitation wavelength of 540-580 nm and the output 593-668 nm wavelength to captures the intensity from mCherry.

Direct hydrogen peroxide administration to the cells was used for screening purposes. Hydrogen peroxide solution in 30% (w/w) in water containing stabilizer from Sigma-Aldrich [68] is diluted using LCIS. A total 300 μM H_2O_2 solution was delivered into the cell culturing well containing 600 μM H_2O_2 after 3-5 frames using a machine-controlled needle to reach the final desired concentration between $10 - 300$ μM. Menadione (1-25 μM), auranofin (500 nM-200 μM) and cyclopiazonic acid (CPA, 20 μM) were used to induce the intracellular H_2O_2 production [5, 6, 7, 66, 69]. The addition of N-acetyl cysteine (NAC) was used to exhaust the residual H_2O_2 prior to the stimulation [70]. For reversibility test, 20 μL dithiothreitol (DTT) was added after saturation H_2O_2 stimulation. The rate of solution delivery was between 4 to 10 mL/minute. We set the needle to inject the H_2O_2 solution at the center of each culturing well and manually chose the field of view in the well to take the images. The selected fields had more than 90 dispersed cells in healthy conditions and the baseline value of these cells were between 100 to 1000 units.

3.4 Image Processing and Analysis

3.4.1 Pre-Processing and Segmentation

All of the fluorescent images were output in TIF format and processed using Python-based algorithms on Google Colaboratory. Rolling-ball algorithm, which was first proposed by Stanley R. Sternberg in 1983, was used to estimate the background intensity [71] for reducing the effect of the uneven background luminescence due to the centered light source during the imaging. Starting by treating the intensity of every pixel as a third dimension, the local background of each pixel is determined by averaging the intensity of a large ball around the pixel [72]. The resulted background intensity was then subtracted from the original images before further analysis.

Three segmentation methods were compared in this thesis: threshold, watershed transformation and Cellpose. All the analysis on sensor characterization were based on the Cellpose segmentation unless further specified. For threshold-based segmentation, a mask was created according to the user-set threshold, which had a default of 50 units to minimize the background noise while avoiding the ROI loss. Any ROI with an average intensity over this threshold value were recorded. A series of image processing methods were performed to the generated threshold mask, including `binary_fill_holes()` and `binary_erosion()` and `binary_closing()`, to integrate the boundaries of the cells. Contours of each ROI were computed using the `find_contours()` method. The watershed transfomration method first set all pixels below 20 intensity to 0, reducing the noise in the background. The original image was first transformed to a map measuring the distance from each pixel in the cell to the background, where the local maximas (the pixel that was furthest to the background) were saved as the markers of ROIs. The flooding from each marker to the boundaries determines the label of each ROI, analogues to the water basin. The method `watershed()` package was then used to perform the flooding step. The Cellpose segmentation was implemented as described in the documentation [4]. All the methods mentioned above were from the `skimage` and `scipy` packages.

3.4.2 Tracking: Cell of Interest Nearest Neighbor

Cell of Interest Nearest Neighbor (COINN) is the name given to the algorithm we developed to track and analyze the single-cell fluorescent readout (Figure. 3.1). The loaded images were assumed to be 4-D, where the four dimensions corresponded to the number of frames (n), channels, image height and image width. Compared to the traditional 3-D time-lapse image, the additional second dimension (channel) depended on the number of output wavelength. In the analysis of HRM63-mCherry ratiometric sensor, the wavelength dimension was 2, where the first and second channels represented the time-lapsed imaging of the cpGFP and mCherry output, respectively.

Cellpose segmentation was first performed for each frame. If the input image was a multi-channel image, the first channel would be used for segmentation. Each 2-D mask computed by Cellpose segmentation were labeled using the method of `label()`, where the order of labeling was determined by the centroid positions.

The generated masks were then used to compute the centroids of each detected ROI using the `regionprops()` method. We used a two-frame window to find the correspondence of cells across the frames. For each frame at time t, the distance d between each i^{th} ROI $C_{t,i}$ in the current frame to each j^{th} ROI $C_{t+\Delta t,j}$ in the next frame were calculated by the Euclidean distance between their x- and y- positions as shown in the equation below:

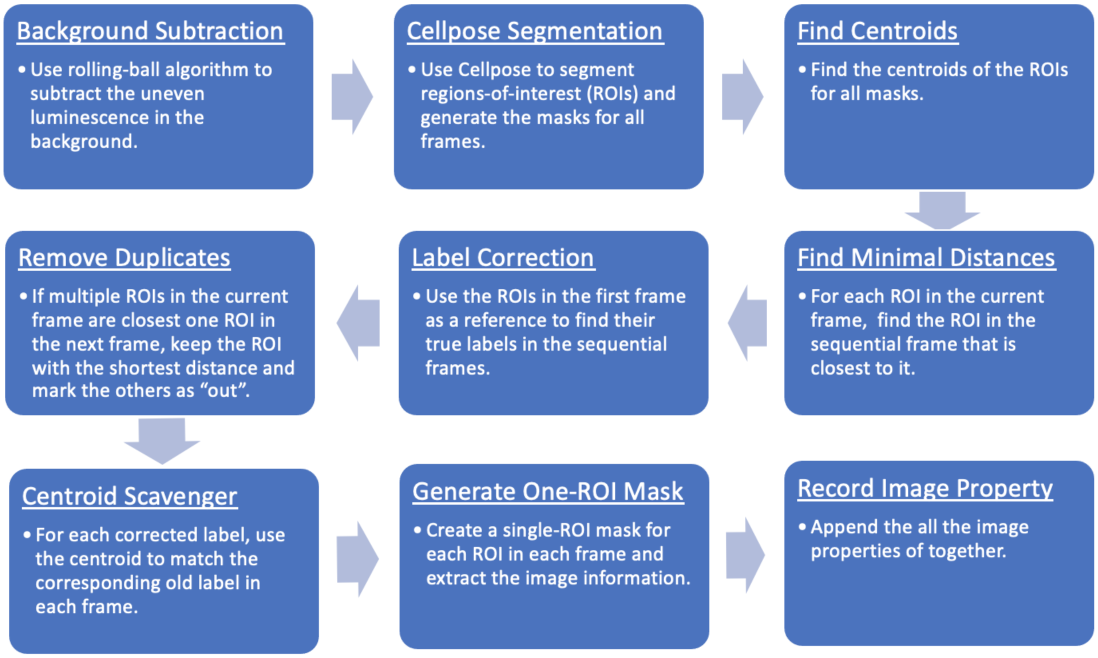

Background Subtraction
- Use rolling-ball algorithm to subtract the uneven luminescence in the background.

Cellpose Segmentation
- Use Cellpose to segment regions-of-interest (ROIs) and generate the masks for all frames.

Find Centroids
- Find the centroids of the ROIs for all masks.

Find Minimal Distances
- For each ROI in the current frame, find the ROI in the sequential frame that is closest to it.

Label Correction
- Use the ROIs in the first frame as a reference to find their true labels in the sequential frames.

Remove Duplicates
- If multiple ROIs in the current frame are closest one ROI in the next frame, keep the ROI with the shortest distance and mark the others as “out”.

Centroid Scavenger
- For each corrected label, use the centroid to match the corresponding old label in each frame.

Generate One-ROI Mask
- Create a single-ROI mask for each ROI in each frame and extract the image information.

Record Image Property
- Append the all the image properties of together.

Figure 3.1: **Schematic showing of the image processing and analysis procedures for single-cell fluorescence analysis in H_2O_2 sensor-transfected cells.** Cellpose segmentation is applied to all frames after background subtraction. The minimal distances of the centroids in the current frame to all ROIs in the next frame are identified. The ROIs from the first frame is then used as a reference to construct a label-correction matrix for the ROIs in the consecutive frames. Duplicated matches of labels are removed by keeping the ROI pair with the shortest distance and marking the others as ”out”. Using the centroids to bridge the labels before and after the correction, a binary mask for each ROI is created at each frame for image property extraction.

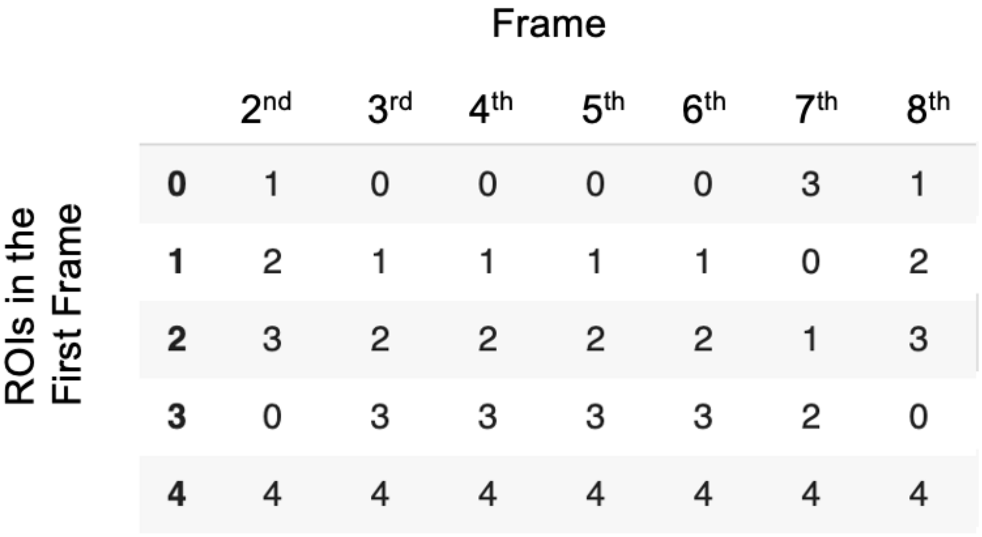

Frame

ROIs in the First Frame

	2nd	3rd	4th	5th	6th	7th	8th
0	1	0	0	0	0	3	1
1	2	1	1	1	1	0	2
2	3	2	2	2	2	1	3
3	0	3	3	3	3	2	0
4	4	4	4	4	4	4	4

Figure 3.2: **Sample label correction matrix of COINN.** For each ROI in the first frame (column), its corresponding labels in the consecutive frames (row) are recorded. Each entry also corresponds to a centroid location (not shown).

$$d(C_{t,i}, C_{t+\Delta t,j}) = \sqrt{(x_{C_{t,i}} - x_{C_{t+\Delta t,j}})^2 + (y_{C_{t,i}} - y_{C_{t+\Delta t,j}})^2}. \tag{3.1}$$

For each $C_{t,i}$, the $C_{t+\Delta t,j}$ that was closest to it would be extracted and recorded with the label of $C_{t,i}$.

The labels of cells in the consecutive frames were then matched to the cells in the first frame based on the proximity and collected to a matrix (Figure. 3.2). The corresponding centroids of these labels were also recorded. Due to the detached cells or the segmentation errors produced by Cellpose, the number of cells in each frame was fluctuating. Since we were using a two-frame window, frames that had less cells than the first frame would contain Not-a-Number(NaN) values, which would be neglected for later image property collection.

To deal with the duplicate cases, where multiple $C_{t,i}$ shared one closest $C_{t+\Delta t,j}$, the distance between each $C_{t,i}$ and the shared $C_{t+\Delta t,j}$ was compared again (Figure.3.3). The

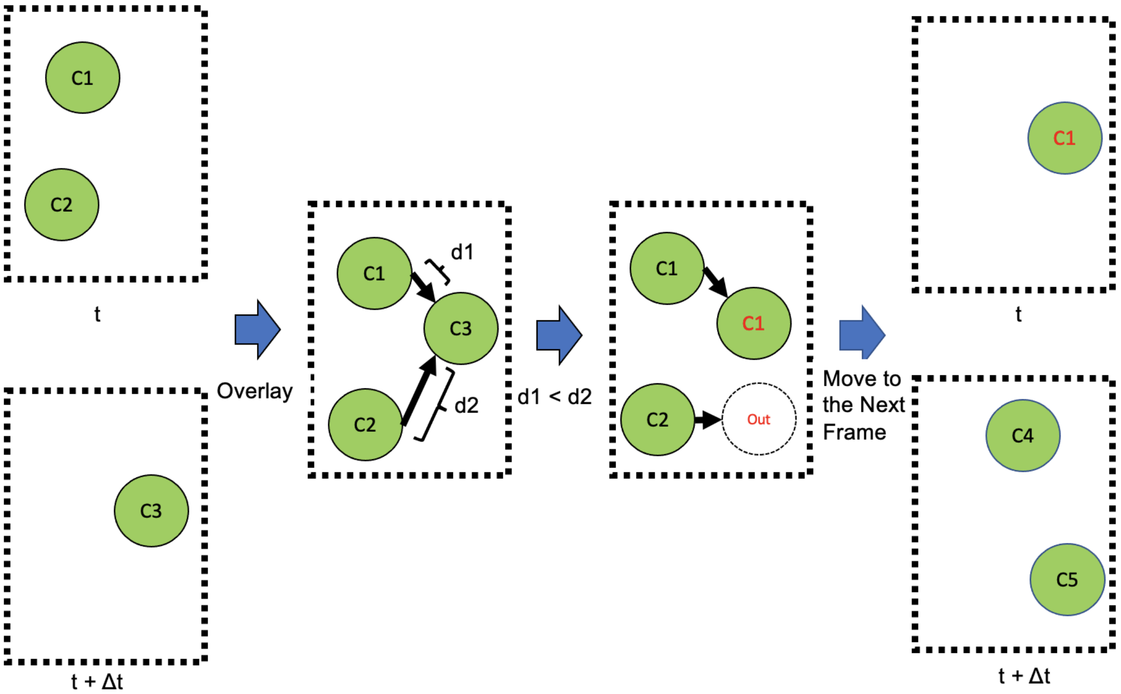

Figure 3.3: **Graphic illustration of duplicate removal in COINN.** If two or more cells in the current frame identify the same cell in the next frame as their ”correct label”, the Euclidean distance between the cells in the current and next frames is compared again. The cell in the current frame with the shortest distance will ”win” the label, and the other cells in the current frame will be marked as ”out”.

$C_{t,i}$ that had the shortest distance among all ROIs proximate to the shared $C_{t+\Delta t,j}$ would be matched. The other $C_{t,i}$ involved in this duplicate removal would be marked as ’out’ in the label correction matrix. Since the first frame was used as the matching reference, the original labels of all ROIs in the first frame were directly appended to the front of the label correction matrix, so that number of columns in the label correction matrix equals to the number of frames in the input image.

Since the centroids before and after the label correction remain consistent, they were used to match the label correction matrix back to the mask. Using the sample label correction matrix in Figure.3.2 as an example, ROI 0 was labeled as 1 in the second frame. The centroid of ROI 1 in the mask of the second frame was then compared to the centroid recorded in the label correction map, ensuring the consistency of tracking. To generate a single-cell mask, all pixels in the second frame other than ROI 1 were set to zero. One thing to note was that Python started labeling the ROIs from 0 when constructing the label correction matrix, but the mask generated by Cellpose started its label from 1. Thus, in the example given above, the pixels within the region of ROI 1 in the second frame should be all labeled as 2. The single-cell mask was then created for each ROI in each frame and used to extract the image properties from them. The collected properties include the detected intensities from multiple channels, normalized intensity to its reduced state, experimental conditions (trail number, stimuli condition, etc) and region properties (cell area, centroids and eccentricity). Only the cells that were present in every frame were used for analysis.

The fluorescent readout of intensiometric sensor was represented by the difference in fluorescence normalized to the fluorescence in the first frame (Equation.2.1). The performance of ratiometric sensor was represented by the ratio between the emission signals of the two wavelengths.

We also verified the nearest-neighbor approach by checking the ratio between the cell displacement across the frames and the mean distance between cells in a single frame. All distances were calculated by the Euclidean distance. The cell displacement across the frames was computed by first averaging the displacement of each ROI across the frames, then averaging the mean displacements of all ROIs. The mean distance between cells in a single frame was calculated by averaging the distance between all pairs of centroids in the first frame. The accuracy of COINN was verified by visually following 5 randomly chosen ROI across all frames.

3.4.3 Classification

Five machine learning-based classification models, or classifiers, including logistic regression (LR), decision tree (DT), k-nearest neighbor (KN), linear discrimination analysis (LDA), support vector machine (SVM) were first used to predict if the individual hiPSC-derived cardiomyocytes demonstrate fluorescent change upon CPA administration. The default parameters from `sklearn` package were used for each model. Image data from six trials of CPA-treated cardiomyocytes were first segmented and single-cell tracked using Cellpose and COINN, respectively.

Seven image properties - F_{610} (mCherry intensity), area, eccentricity, major axis length, orientation, and x- and y-positions of the centroid were first separately used to train the given models. For each trial, the data matrix was given by the size of `[number of ROIs * number of frames]` filled by the designated image property. Each ROI was given a label of either 0 or 1, where 0 represented low-response cells and 1 represented at least 1% of fluorescent change upon CPA administration. The data matrix and labels of each trial were then appended together and randomly shuffled by ROIs, resulting a final data matrix of size `[(number of ROIs * number of trials) * number of frames]` and a label list with the same length as the row number of the data matrix. The splitting ratio between the training and testing groups was empirically set to 9:1 based on the total number of row of the data matrix. The classification was done 10 times with the training and testing groups split from randomly shuffled data matrix at each time. The prediction accuracy of each model and each image property was then computed by taking the average of the 10 iterations.

The same image features were then used together to train the model with the highest accuracy in classifying the time-lapsed data. The data matrix for the all-parameter classification is of size `[(number of ROIs * number of trials) * number of features]`. The image features of each ROI were taken from the first frame of each trial. All the following splitting and validation followed the same procedures as the time-dependent classification.

3.5 Statistical Analysis

All error bars used in this thesis represent the standard error of the mean (SEM). Significance was determine using two-tailed t-test with a 95% or greater confidence level. The variance of data was represented by the equation shown below:

$$S^2 = \frac{1}{n-1}\sum(x_i - \bar{x})^2 \tag{3.2}$$

where S^2 is the sample variance, n is the total number of samples, x_i is the i_{th} observation and $\bar{x}$ is the sample mean. Levene's test was used to test the equal variance of the populations with the assumption of skewness.

Chapter 4

RESULT

This section includes the results from the procedures described in the previous section, primarily focusing on the experimental evidence of HRM63 sensor characterization and computational result from the cell segmentation and single-cell tracking methods. The results provide new insights towards the understanding of HRM63 functionality, as well as the pipeline of image analysis in GEFI detecting H_2O_2.

4.1 Sensor Characterization

4.1.1 Photoactivation

HRM63 is specific to its excitation wavelength, making it a suitable sensor to be used together with the biomarkers of other colors. To allow the co-application of multiple sensors, the generated probes should only be activated by wavelength within its excitation wavelength band. It means HRM63 and HyPerRed should only exhibit fluorescent change when they are stimulated by 488 nm and 597 nm wavelength, respectively. However, with its excitation wavelength of 597 nm constitutively exhibits fluorescence on the background, HyPerRed displays fluorescent peaks along with the periodic stimulation of 488 nm (Figure. 4.2.a). HRM63 demonstrates no obvious fluorescent activation with the periodic 597 nm stimulation (Figure. 4.2.b). This result indicates that HRM63 can be used along with other probes of different wavelengths without having an affected fluorescent readout.

4.1.2 Reversibility

We also verify the reversibility of HRM63 *in cyto*. Dithiothreitol (DTT) acts as a protective reagent for -SH groups [73], quantitatively reducing the formation of disulfide bridges by maintaining the monothiols in their reduced states [74, 75]. By first stimulating the HRM63-transfected HEK293 cells to its saturation state using 300 μM of H_2O_2, we observe that adding 20 μM of DTT induces a rapid drop of the fluorescent output down to the basal level (Figure. 4.2.c). A minimal relapse of fluorescence occurs after the H_2O_2 exhaustion due to a small amount of residual H_2O_2. Adding a second wash of H_2O_2 after the DTT-induced H_2O_2 exhaustion triggers a new peak of fluorescent output (Figure. 4.2.d). Both the dynamic and amplitude of the second fluorescent peak are similar to these in the first stimulation. Thus, this results shows that the fluorescence of HRM63 is reversible *in cyto*, demonstrating the application of this sensor in the studies that require multiple times of stimulation.

4.1.3 Subcellular Compartment Sensitivity

We examine the sensitivity of HRM63 in the cellular compartment. The variants of HRM63 and HyPerRed expressed in the mitochondria are designed to compare to the cytoplasm- expressing variants. Cytoplasm-expressing HRM63 demonstrates a higher fluorescent output compared to the mitochondria-expressing variant, showing the sensor capability of distinguishing small H_2O_2 variation occurred within the same cell (Figure. 4.2.e). Both the cytoplasm- and mitochondria-expressing HyPerRed exhibits minimal fluorescent output. Both the loss-of-function (LoF) variants of HyPerRed and HRM63 are introduced with mutation C199S to prevent the OxyR-RD from interacting with H_2O_2 [11]. Neither of the LoF variants demonstrate any fluorescent changes upon H_2O_2 stimulation, indicating that the fluorescent output is not affected by the environmental changes in physiological condition.

4.1.4 Volumetric Control

We verify the fluorescent output of HRM63 by designing a ratiometric sensor that fuses a constitutitively red fluorescent protein named mCherry to the non-flexible region of the sensing domain of HRM63 (Figure. 4.1), inspired by the GCaMP-mCherry design in the calcium protein indicators [76]. This ratiometric variant enables the normalizing analysis of HRM63, validating the comparison between the green fluorescent output of HRM63 with the red readout from HyPerRed. The comparison of the fluorescent performance of HRM63-mCherry and HyPerRed as a function of H_2O_2 gradient demonstrates the high sensitivity

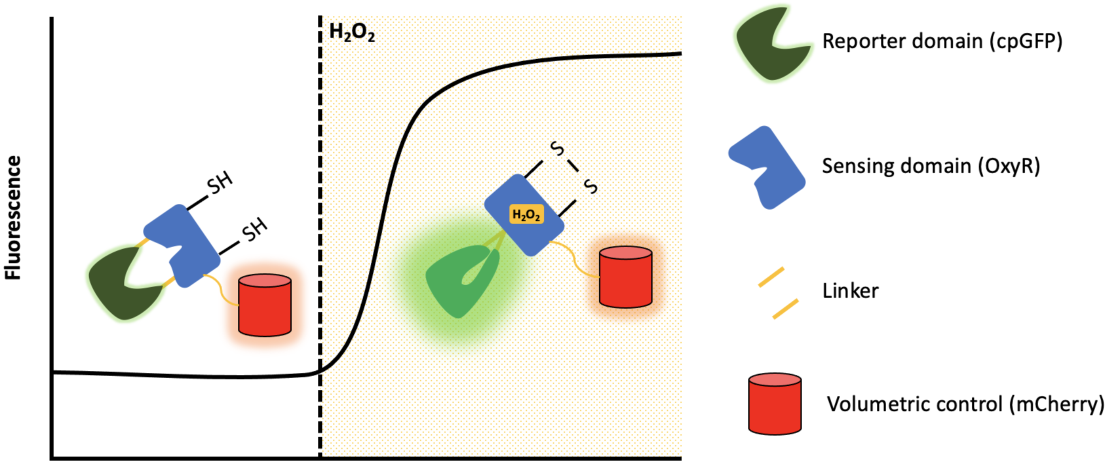

Figure 4.1: **Schematic showing of HRM63-mCherry ratiometric sensor.** A constitutively expressing mCherry is fused to the non-flexible region of the sensing domain, serving as a volumetric control over the protein expression of the sensor.

of HRM63 at low H_2O_2 concentration, shown by the 100% of fluorescent change upon 8 μM H_2O_2 stimulation, which is ten-fold higher than the 10% fluorescent output of HyPerRed (Figure. 4.2.f). The maximal fluorescent output of HRM63 is 200% upon 300 μM H_2O_2 stimulation, demonstrating two-fold higher performance compared to HyPerRed.

HRM63-mCherry variant also serves as a volumetric control over the expression level of the sensor. We investigate the performance of HRM63-mCherry as a function of menadione concentration, a precursor for redox-cycling-triggering vitamin K synthesis [5]. By stimulating the sensor-transfected cells with various concentration of menadione and measuring the green and red values of cells for 10 hours, we discover that the protein expression level slowly increases by around 50% in all trials (Figure. 4.2.g). This result indicates the necessity of having a volumetric control to not only account for the variance in protein expression level among the cells, but also take the growing protein expression in long-term imaging into consideration. Meanwhile, it also shows that HRM63-mCherry variant is sensitive enough to distinguish the intracellular production of H_2O_2 induced by the cellular mechanism agonists.

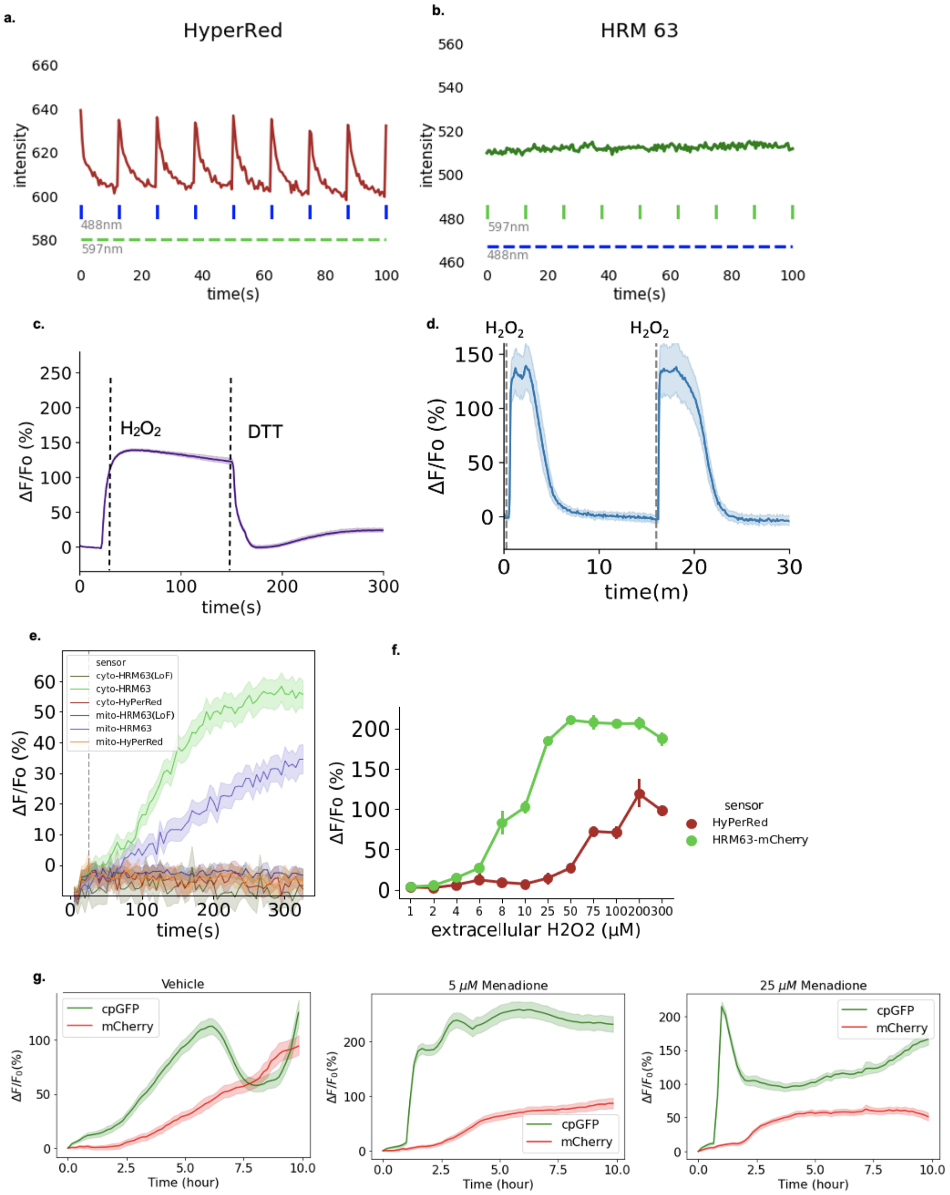

Figure 4.2: **HRM63 sensor characterization. a-b.** Photoactivation of HyPerRed and HRM63 by the wavelengths outside of their excitation wavelength range. **a.** HyPerRed, with 597 nm constitutively on and periodic 488 nm flashes. **b.** HRM63, with 488 nm on the background and periodic 597 nm flashes. **c-d.** Reversibility of HRM63. **c.** By adding 20 mM of dithiothreitol (DTT), HRM63 can be returned to its reduced status. **d.** HRM63 can be oxidized again by a second wash of H_2O_2 after been reduced by DTT. **e.** Fluorescent comparison of HRM63 and HyPerRed transduced in cytoplasm and mitochondria. Transfected HEK293 cells were stimulated with 10 μM menadione. cyto = cytoplasm. mito = mitochondria. LoF = Loss-of-function variant. **f-g.** Performance of ratiometric HRM63-mCherry sensor in HEK293 cells. **f.** Performance comparison between HRM63-mCherry and HyPerRed as a function of H_2O_2 concentration gradient.**g.** Ratiometric fluorescent reading of HRM63-mCherry as a function of menadione concentration gradient.

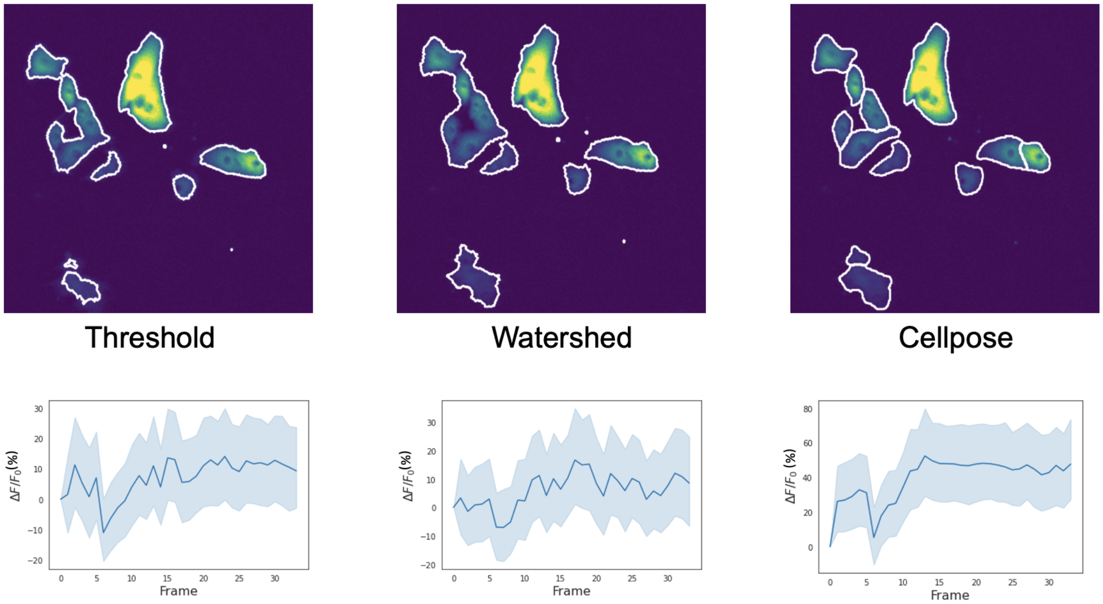

Figure 4.3: **Comparison of the segmentation result (top) and intensity values (bottom) collected from the masks created by the threshold-based, watershed transformation and Cellpose methods.** Though all three methods were able to detect cells in the sample HRM63-transfected hiPSC-derived cardiomyocytes, Cellpose demonstrates better delineating accuracy and separation result on the touching cells. The extracted intensity using Cellpose segmentation also provides a cleaner trend reflecting the fluorescent change.

4.2 Computational Pipeline of Evaluating Genetically Encoded H_2O_2 Probe

4.2.1 Cellpose Segmentation Improves the Image Data Extraction

In our prior analysis of fluorescent images, we typically used the threshold-based method through ImageJ because it was computationally efficient and easy to implement. Watershed transform is also a popular and easy-to-use cell segmentation approach for many ongoing studies of cell biology [51, 52]. We then use HRM63-mCherry-transfected hiPSC-derived cardiomyocytes treated with 20 μM CPA at the fifth frame as a sample image to verify the performance of the segmentation methods. As shown in Figure.4.3, HRM63-mCherry variant can successfully express in the cardiomyocytes, demonstrating its application in the study of monitoring H_2O_2-production in cardiovascular mechanism. The cpGFP channel of cells in the reduced state is taken at the first frame to compare the segmentation results. Both threshold-based and watershed transformation methods mentioned above are able to separate the cells from the background, but the threshold-based method fails to delineate the outer boundaries, and watershed transform approach cannot separate the cluster of touching cells.

Cellpose method demonstrates better segmentation of the touching cells in HRM63-transfected hiPSC-derived cardiomyocytes compared to the threshold-based and watershed transformation methods, enabling the accurate extraction of fluorescent readout as well as the single-cell tracking in the later analysis. Compared to the two segmentation methods described above, the segmentation result from Cellpose demonstrates better performance in both the delineation of cell contours and the separation of multiple touching cells. The touching-cell separation of Cellpose can be credited to the flow gradient vector representation of the cell and the additional two-channel (cytoplasm and nucleus) image dataset used to train the neural network in Cellpose [4, 77]. In terms of variant screening and sensor characterization of H_2O_2 sensor, the enhanced cell segmentation reduces variance due to the interference of the background luminescence, providing a more trustworthy representation of oxidation level (Figure.4.3). The separation of touching cells provide more accurate information on single-cell identities, aiding the studies on cell-to-cell difference.

One problem of using Cellpose segmentation is its long processing time due to the computational complexity of neural network. The time to compute the Cellpose segmentation result on a regular workstation (Intel(R) Core(TM) i5-6300HQ CPU, 2.30 GHz, 4 GB RAM, Windows 10 Professional) is approximately 124 seconds per single frame of $1200 * 1200$ resolution. For a typical ten-minute imaging with an exposure time of 100 milliseconds for variant screening, each image stack will have 600 frames, and it will be a total of 14400 2-D images to process for an experiment with a full 24-well cell-culturing plate. The segmentation processing of all the images is almost 500 hours. Thus, we come up with two approaches to conquer this computational complexity. The preferred approach is to use online processing server. We choose to use Google Colaboratory, which is a Python-based notebook that provides access to GPU and TPU from Google's cloud server. It reduces the time of segmentation to around 4 seconds per frame, which is 60-fold less than using the

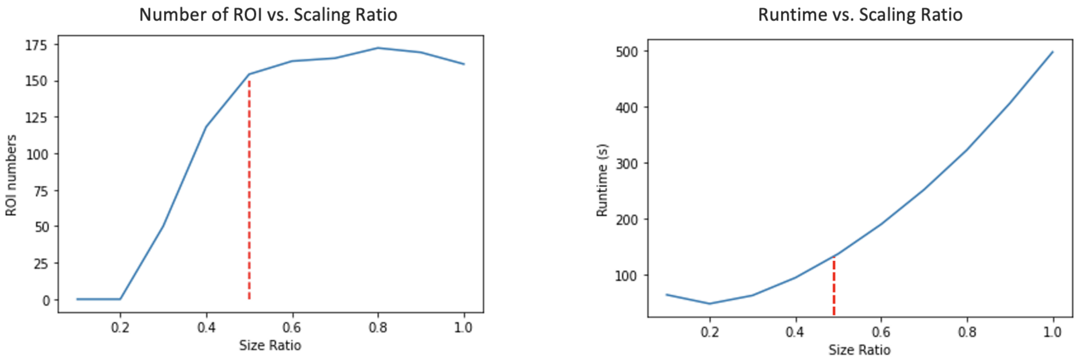

Figure 4.4: **Trade-off between ROI loss and computational time reduction.** Reducing the rescale factor causes the ROI loss but also reduces the computational time. Setting the rescale ratio to 0.5 (red dashed line) achieves the best balance between the ROI numbers and computational time.

regular CPU from the workstation.

An alternative approach is to scale down the input image, reducing the data unit for processing. Cellpose requires an optional input parameter named `rescale` that determines the resizing ratio of the input image. The output mask is still the same size as the original image. To validate the information loss during resizing, we use Cellpose to segment the image of HyPerRed-transfected HEK293 cells in the reduced state with the rescale ratio from 0.1 to 1 and compare the number of detected ROIs and computational time. The result suggests that while the computational time increases exponentially as the rescale ratio increases from 0.1 to 1 by an increment of 0.1, the trend of detected ROIs becomes constant after the rescale ratio reaches to a certain threshold. It shows that rescaling the original image to its 50% saves half of the computational time but only causes minimal ROI loss. Thus, this rescaling approach can be used to reduce the computational time when the advanced processing unit is not available or the input image has high image resolution.

4.2.2 Single-Cell Tracking Visualizes the Cell-To-Cell Difference

Using label correction and duplicate removal, COINN enables the single-cell tracking based on Cellpose segmentation. Though Cellpose demonstrates excellent delineating accuracy and clean separation of touching cells in 2-D fluorescent cell segmentation, it fails to provide the temporal correspondence of cells in the time-lapsed imaging data. Additionally, due to the position-based consecutive labeling of the mask, if Cellpose fails to detect one cell in a frame, or a floating dead cell that enters or leaves the field of view, all the following cells would be mislabeled. As shown in Figure.4.5, Cellpose segmentation identifies the cell at the top right corner as one cell, but in the following frames the same region is recognized as two touching cells. The consecutive labeling then changes for all the ROIs located under the mislabeled cell. Using the label-correction method, we provide the time-lapsed correspondence to the cells by finding their true labels based on their centroids in all frames. Neither the segmentation error nor cell motion affects the labeling of the same cell across different frames. We then validate the use of nearest-neighbor approach in hiPSC-derived cardiomyocytes by calculating the ratio between the cell displacement across the frames and the mean distance between cells in the first frame. The resulted ratio is $1.56/615.76 \approx 0.0025$, which is smaller than the threshold of 0.05 set by Ponti *et al.* [63], suggesting that the nearest-neighbor tracking is possible for the type of cells and imaging that we use.

Thus, the time-lapsed image property of single cells can be extracted by simply following the corrected labels (Figure. 4.6). Tracking the fluorescent readout of the first six cells segmented by Cellpose shows that the position-based consecutive labeling causes the disconnected time-lapsed intensity, whereas the label correction of COINN leads to the correct single-cell temporal correspondence. The result of tracking shows the cell-to-cell difference in terms of fluorescent readout. All six segmented cells are proximate to the top edge of the image, which implies similar level of luminescent noise from the background and similar rate of receiving the agonist that diffuses from the center of the cell culturing well, but they demonstrate distinct dynamic in response to the CPA administration. The cell with the highest initial green intensity also exhibits the highest fluorescent change upon the CPA

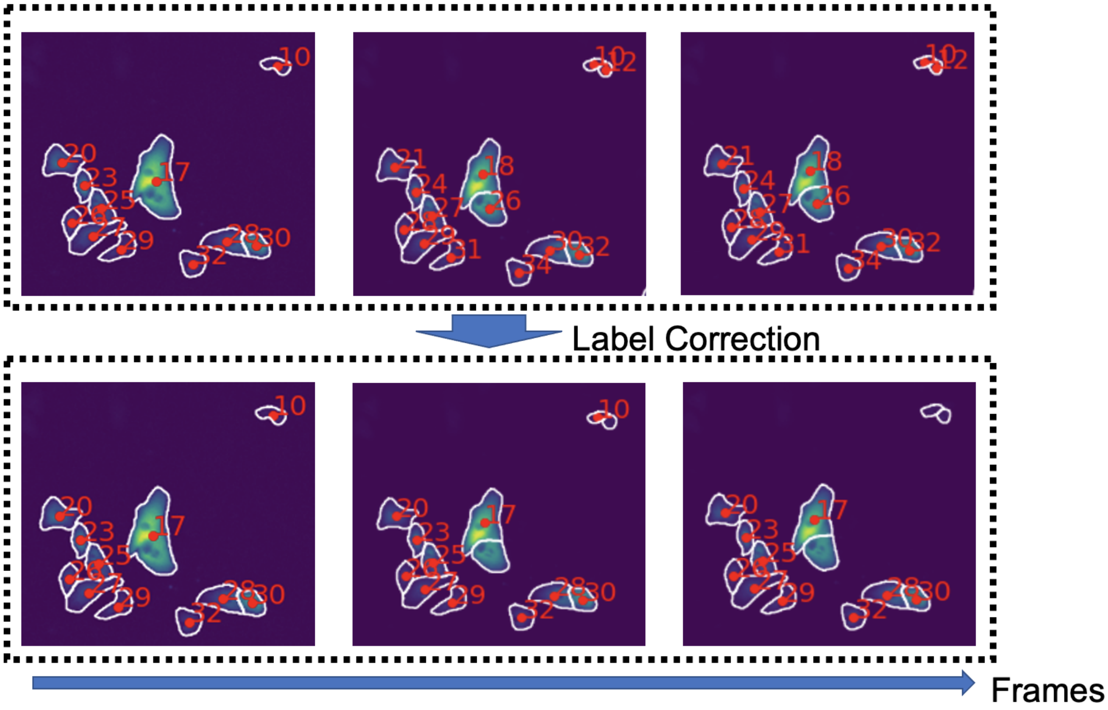

Figure 4.5: **Label correction maintains the temporal consistency of the mask labels.** The segmentation errors on touching cells produced by Cellpose leads to the shuffled labeling of all the consecutive ROIs (top). Label correction of COINN ensures the correct cell labeling for single-cell tracking in time-lapsed images (bottom).

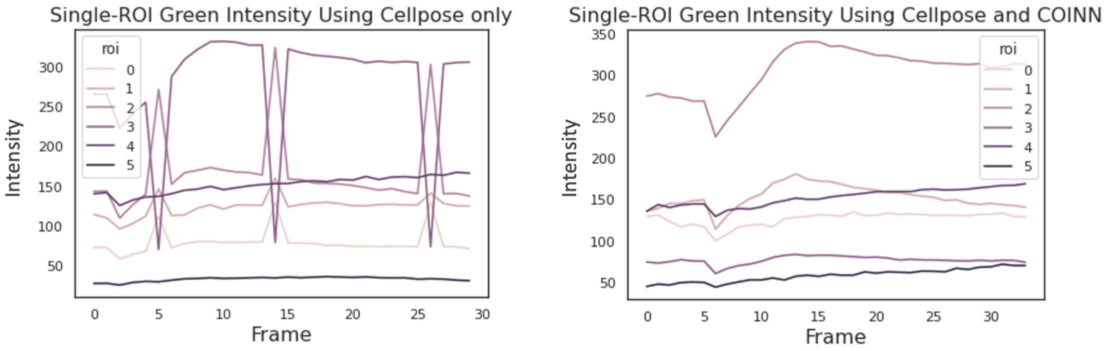

Figure 4.6: **COINN enables the single-cell tracking of image properties.** The shuffled labeling from Cellpose segmentation leads to inaccurate temporal correspondence of fluorescent readout of single cells (left), which can be corrected by COINN (right).

Trials	1	2	3	4	5	6
Percentage of low-response cells in CPA-treated hiPSC-derived cardiomyocytes (%)	6.12	35.29	58.62	13.89	65.00	4.00

Table 4.1: **Percentage of hiPSC-derived cardiomyocytes that demonstrate less than 1% maximal fluorescent change upon the administration of CPA.** The low-response portion in different trials spans a large range.

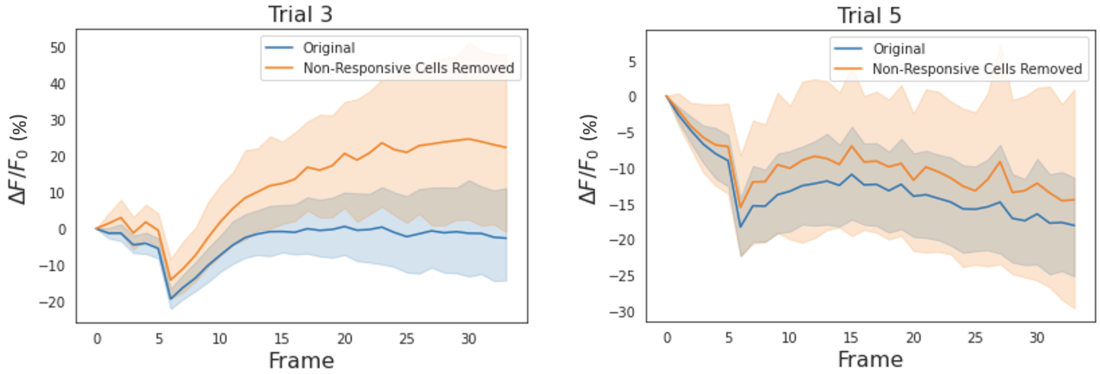

Figure 4.7: **Removing the low-response cells from the data improves the fluorescent readout.** Variance increases as a result of the reduction of total number of data points.

administration. The cells that are initially dimmer tend to be low-response to the agonist.

To verify the portion of low-response cells in the CPA-treatment group, we implement COINN on six CPA-treated trials and calculate the percentage of low-response cells that exhibit less than 1% of maximal fluorescent change upon CPA administration (Table.4.1). CPA as a SERCA inhibitor prevents the recycling of Ca^{2+} into SR, leaving excessive Ca^{2+} in the cytoplasm that disrupts the mitochondrial metabolism and induces oxidative stress [24, 66]. For consistency, the cells that demonstrate more than 1% of maximal fluorescent change are represented by "responsive cells" in the following context. The result varies from 4% to 65%, demonstrating a large trial-to-trial difference in response to the CPA administration.

By removing the low-response portion from the trials 3 and 5 that contain over 50% of low-response cells, the overall fluorescent change of both trials noticeably increases (Figure.4.7). We then quantify the data variance by calculating the population variance of all ROIs in each frame using Equation.3.2. Assuming equal variance in each frame, the pooled variance of all frames increases from 0.23 to 0.28 in trial 3 and from 0.13 to 0.15 in trial 5 after the removal of low-response cells, as an expected outcome from removing more than half of the data points.

4.2.3 Volumetric Control Provides a More Comparable Representation of Oxidation Level for Intensiometric Sensor

As described in the previous section, the mCherry fused to the non-flexible region of OxyR-RD serves as a protein-level control for HRM63. During the variant development, we observe that the variance among the experiments due to the biological factors is significant. It does not only cause inconsistent results, but also mislead us in the following experiments. Though we are able to minimize its effect by controlling a few factors, such as the temperature during the imaging and cell culturing, the residual problems can still sabotage the experimental results and therefore reduce the efficiency of variant development. By adding a volumetric control to the intensiometric sensor HRM63, the changes in the surrounding environment of the sensor-transfected cells will project to both the reporter domain (cpGFP) and the control (mCherry) that are proximate to each other when transfected to cells. Thus, we hypothesize that using the ratio between the intensity of cpGFP and mCherry can better represent the oxidation state of the sensing domain by normalizing the variance due to unpredictable biological factor.

We first use the ratiometric reading to represent the H_2O_2 production in cardiomyocytes. As shown in Figure.4.8, the elevated fluorescent result first demonstrates that HRM63 is capable of capturing the intracellular H_2O_2 produced in hiPSC-derived cardiomyocytes triggered by CPA. To distinguish the output from cpGFP and mCherry, we call them "F_{509}" and "F_{610}", respectively. The ratiometric reading from both wavelengths is "F_{509}/F_{610}". We originally take the first frame of F_{610} as the only control for the entire imaging sequence,

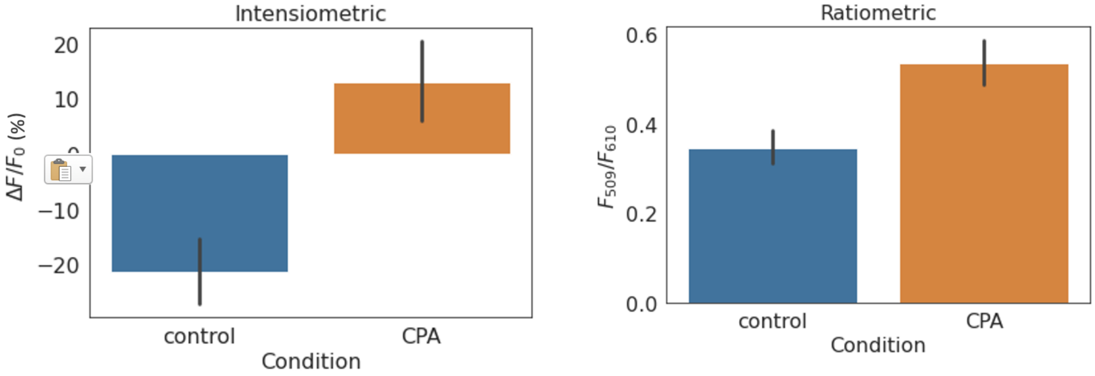

Figure 4.8: **Comparison of the intensiometric and ratiometric output in the last frame of hiPSC-derived cardiomyocytes triggered by CPA.** $\Delta F/F_0$ is the percentage change of cpGFP emission intensity from the baseline values. F_{509} and F_{610} refer to the emission intensity of cpGFP and mCherry, respectively.

but we then discover that the expression level of HRM63-mCherry increases across frames in long-term imaging (Figure.4.2.g). Thus, we alter our imaging pipeline to capture both the F_{509} and F_{610} for each frame. During the segmentation, we empirically choose the cpGFP channel as the reference to generate the masks for both F_{509} and F_{610}. Both the normalized F_{509} ($\Delta F/F_0$) and ratiometric reading (F_{509}/F_{610}) can represent the sensor oxidation level in response to the CPA administration.

Using the pixel-wise ratio between cpGFP and mCherry intensity in the time-lapsed imaging of sensor-transfected cells reduces variance in fluorescent readout. As mentioned in the previous section, we hypothesize that the ratiometric reading normalizes the unknown biological factors during both short- and long-term imaging, leading to more homogeneous fluorescent outputs. In order to test the hypothesis, we calculate the pooled variance of all frames from each trial of CPA-treated hiPSC-derived cardiomyocyte and compute the average variance from the first three trials of both the control and CPA-treated groups. We also calculate the variance from the data of HRM63-mCherry-transfected HEK293 cells stimulated with menadione and auranofin. Auranofin serves as a thioredoxin reductase inhibitor that stimulates the mitochondrial production of H_2O_2 [6, 7]. As shown in Table.4.2,

Agonist	**Cell Type**	**Final Concentration (μM)**	**Average Variance of Three Trials**		
			$\Delta F/F_0$ **of** F_{509}	F_{509}/F_{610} **ratio**	$\Delta F/F_0$ **of** F_{509}/F_{610}
Control	hiPSC-derived cardiomyocytes	0	0.22	0.17	0.15
CPA	hiPSC-derived cardiomyocytes	20	0.21	0.22	0.17
Control	HEK293	0	0.70	0.37	0.36
Auranofin	HEK293	0.5	1.56	0.55	0.56
		2	2.94	0.92	0.93
Menadione	HEK293	1	1.21	0.56	0.58
		5	0.97	0.57	0.60
		10	0.79	0.50	0.47
		25	1.53	0.62	0.69

Table 4.2: **Comparison of the variance of using $\Delta F/F_0$ of F_{509}, F_{509}/F_{610} ratio and $\Delta F/F_0$ of F_{509}/F_{610} as the measurement of fluorescent output in HRM63-mCherry-transfected cardiomyocytes and HEK293 cells.** $\Delta F/F_0$ of F_{509}/F_{610} is the F_{509}/F_{610} normalized to the baseline ratio before adding any agonists. Each variance is computed by the average variance from three trials of the same conditions. Using the F_{509}/F_{610} ratio or normalized ratio to represent the fluorescent change reduce the variance among the cells.

the variance of fluorescent outputs among the cells is reduced when using F_{509}/F_{610} ratio and $\Delta F/F_0$ of F_{509}/F_{610} as the measurement instead of the $\Delta F/F_0$ of F_{509}. This variance reduction is more evident in the data from HEK293 cells, where most of the variance in using F_{509}/F_{610} ratio and $\Delta F/F_0$ of F_{509}/F_{610} is only half or even third of the variance of using the $\Delta F/F_0$ of F_{509} as the fluorescent measurement.

The combination of volumetric control and single-cell tracking enables the filtration of cells with aggregated and low-response proteins. Protein aggregation refers to the biological phenomenon when the proteins accumulate and clump together, favoring its most thermo-

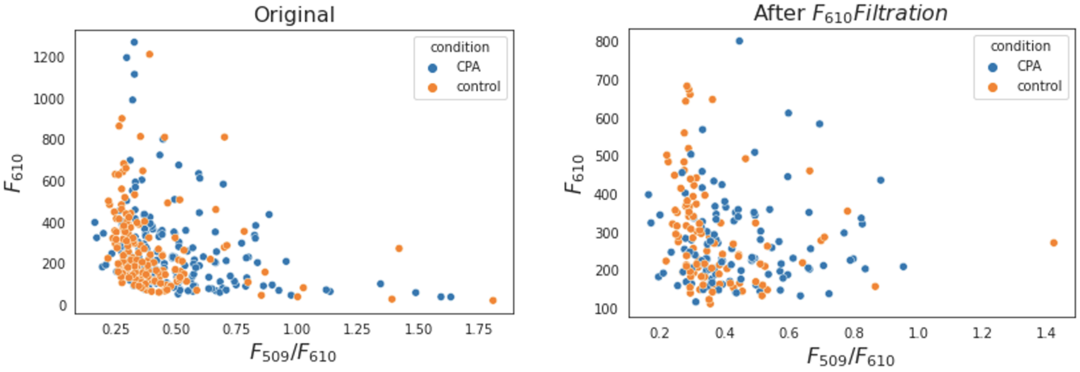

Figure 4.9: **Removal of the cells with extreme F_{610} values improves the separation of conditioned data.** Both the cell-to-cell difference and fluorescent response in CPA-treated group can better be visualized after the removal of low-response and protein-aggregated cells.

dynamical state [78]. The aggregation of GFP strongly correlates to the fluorescent protein concentration in the targeted area [79]. In terms of sensor-transfected cells, high protein expression represented by large F_{610} can be a sign of aggregation, potentially introducing artifacts to the fluorescent readout. Moreover, as shown in Figure.4.6, the ROIs that have a lower initial value tend to be less responsive to the CPA administration. Thus, we hypothesize that the fluorescent readout of ROIs with extreme levels of fluorescent protein expression are more likely to experience drawbacks. We then rank the CPA-treated hiPSC-derived cardiomyocytos in the last frame based on their F_{610} and apply filter to the top (high F_{610} value) and bottom (low F_{610} value) of the list. The percentage of filtration is determined empirically based on the visual inspection. As shown in Figure.4.9, removing the cells with top 10% and bottom 35% F_{610} values better visualizes the distributive difference between the CPA-treated and control groups. Each dot represents a single ROI in the last frame. Both the CPA-treated and control groups demonstrate positive skewness in the distribution of F_{610} values. The filtered plot shows that the cells in the control group are confined to a smaller F_{509}/F_{610} range of approximate 0.3 - 0.5, whereas the cells from the CPA-treated group range from 0.2 to 1.0 F_{509}/F_{610} ratio. Thus, this representation of difference in fluorescent readout accounts for the cell-to-cell difference in protein expression level, providing a more reliable and quantitative comparison between the treatment and control groups. The p-values for the original and F_{610}-filtered data are $8.99e^{-}5$ and $2.26e^{-}3$. While both data sets demonstrate statistical significance, the elevated p-value in the filtered group is expected as the number of data points are reduced.

4.2.4 Using Machine Learning-Based Classification to Predict the Cell Responsiveness Upon Agonist Administration

As described in the previous section, the purified cardiomyocytes can provide distinct fluorescent outputs. The low-response cells upon CPA administration exist in all six trials of CPA-treated HRM63-mCherry-transfected hiPSC-cardiomyocytes. Since the mechanism behind this phenomenon remains unknown, identifying the shared characteristics by the low-response cells can help us to better interpret the fluorescent readout from the H_2O_2 sensors. Thus, we choose seven image features that can be extracted using COINN and train five different machine learning-based classification models to investigate the correlation between these features and cell fluorescent response. Six features (area, eccentricity, max axis length, orientation and x- and y-position) are suggested by Al-Kofahi *et al.* to identify cells in a cell segmentation method [62], implying their potential to describe the cell conditions. The five classification models (LR, DT, K-NN, LDA and SVM) are suggested in a review of cell classification using numerical features [45]. As shown by the result in the volumetric control section, the protein expression level represented by the mCherry intensity is also critical to the fluorescent performance of individual cells. Thus, F_{610} is also used along with other six features.

The combination of SVM model and y-position feature produces the highest prediction accuracy. As shown in Figure.4.10, the level of prediction accuracy is similar among the used models and image features. The SVM model and the feature of y-position demonstrate slightly higher prediction accuracy of 79.1% than the other model/feature pair, surpassing the overall average prediction accuracy of 67.4% (all accuracy values shown in Table.A.2). The kernel of SVM model is tuned to the radial basis function (RBF) to achieve the best

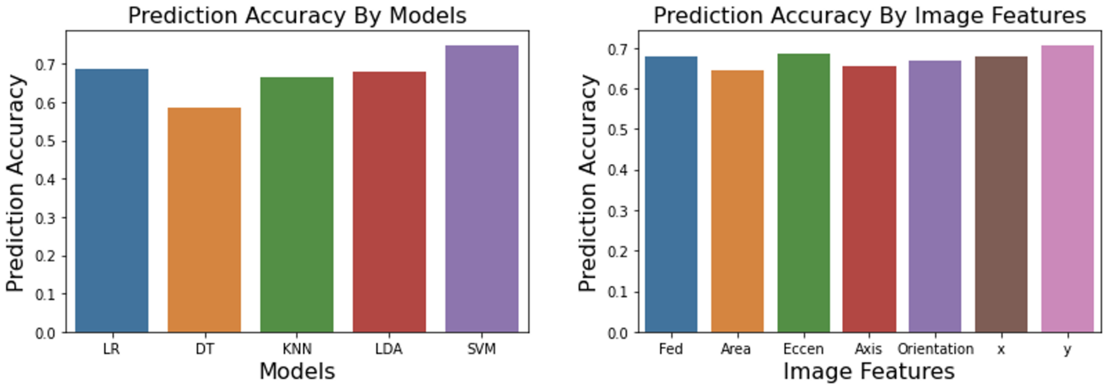

Figure 4.10: **Average prediction Accuracy of the models and image features in the classification of whether HRM63-mCherry-transfected cardiomyocytes respond to CPA administration.** Prediction results are similar in all model/features. The combination of SVM model and feature of y-position demonstrates the highest prediction accuracy.

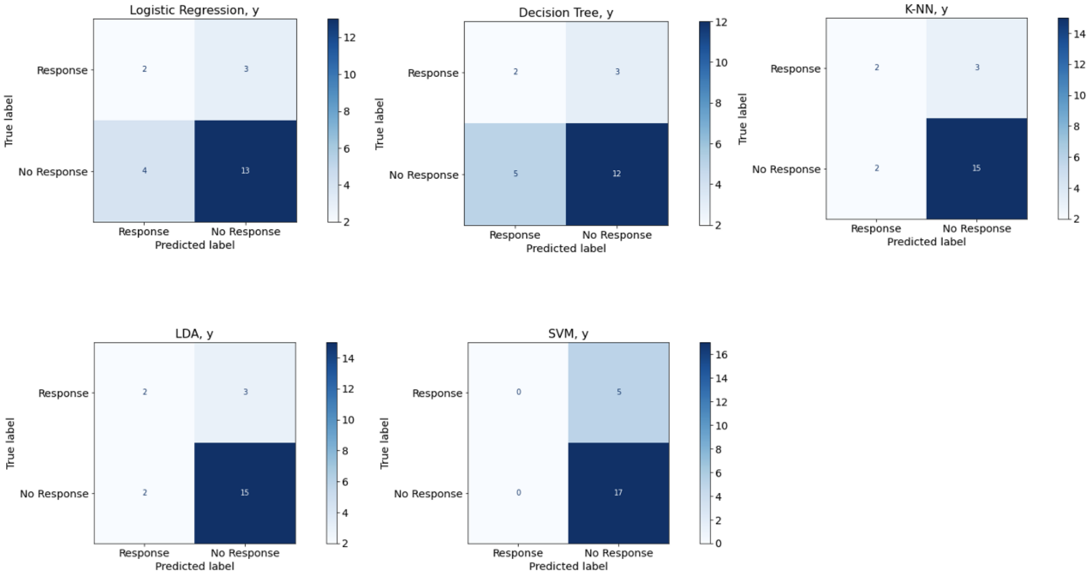

Figure 4.11: **Confusion matrix of different models in the fluorescent response classification.** The image feature used to train the models is the y-position of cell centroid. The SVM classifier demonstrates the lowest false negative rate.

performance (Figure.A.3). It shows that SVM method is advantageous in non-linear classification. We also compare the confusion matrix of five classifiers using the y-position as the training feature (Figure.4.11). The SVM model demonstrates the lowest false negative rate compared to other models, but it fails to identify the cells that demonstrate fluorescent response. Indeed, all models demonstrate higher accuracy in classifying non-responsive cells compared to the responsive cells. This result can be due to the uneven proportion of the response and non-response groups in the testing set. An alternative explanation is, since we use time-lapsed data as the input data matrix, the features of non-responsive cells follow the similar patterns, while the responsive cells demonstrate various characterization. Using the time-independent data matrix where each ROI is described by all seven features in the first frame of each trial provides an average accuracy of 72.3%, lower than using the time-dependent data.

Chapter 5

DISCUSSION

This section provides the interpretation on the results described in the previous chapter. We use sensor characterization to demonstrate the advantages of using HRM63 in *in cyto* H_2O_2 monitoring and describe the significance of developing computational pipeline for time-lapsed image analysis of H_2O_2 sensors. The limitations and future direction are also included for the scope of this thesis.

5.1 Sensor Characterization

The experiments from this section validates the application of HRM63 in the studies involving H_2O_2 monitoring. Expressing HRM63 in different cellular compartments also demonstrates its capability to distinguish intracellular H_2O_2 gradient. The ratiometric readouts from HRM63-mCherry variant provide more consistent fluorescent output, validating its high performance. Sensor characterization of HRM63 also demonstrates the sensor reversibility and consistent excitation spectrum.

For the scope of this thesis, the *in cyto* fluorescent output provides strong evidence for our sensor performance. In order to prepare the sensors for future *in vivo* H_2O_2 monitoring, we need to verify its performance in more cellular mechanisms. The results of inducing the intracellular H_2O_2 production using menadione and auranofin in the HEK293 cells expressing HRM63-mcherry demonstrates a distinguishable output upon various concentration of H_2O_2 stimulation. The CPA-induced fluorescent readout from the HRM63-mCherry-transfected hiPSC-derived cardiomyocytes shows the application of our sensor in capturing transient production of H_2O_2 in the study of ischemia and heart perfusion mechanism. We will expand the application of HRM63 in different cell types and mechanisms, exploring its potential as an effective intracellular H_2O_2 probe.

Though HRM63 as a green variant demonstrates high fluorescent output and fast responding dynamic, the spectrum of green fluorescence has poor penetration through deep tissue, limiting its *in vivo* application in mammals. It guides us towards the next step of designing sensor that uses near-infrared red (NIR) fluorescent protein as the reporter domain. The low light-scattering and auto-fluorescence of NIR fluorescent protein with an optical spectrum of 650–900 nm enables the deep-tissue imaging [80]. There have been multiple protein sensors coupling with fluorescent proteins with red-shifted chromophore [80, 81], but the application of NIR fluorescent proteins in detecting H_2O_2 has not yet been fully investigated. Thus, we will explore the possibility of coupling NIR fluorescent protein to our current design, facilitating the H_2O_2 detection *in vivo.*

5.2 Computational Evaluation

5.2.1 Cellpose Segmentation

Compared to the traditional threshold-based and watershed transformation segmentation methods, Cellpose fulfills our need using its high delineating accuracy and separation of touching cells. Though the computational complexity of Cellpose requires advanced processing units, we have come up with solutions of using the online processing units on Google Colaboratory and rescaling the input image to enable the frequent use of this method. Overall, among many existing segmentation method for cells, Cellpose is an appropriate tool to extract image values.

We acknowledge the segmentation errors resulted from Cellpose method. The segmentation result of images with low SNR ratio is often error-prone. For the fluorescent imaging during H_2O_2 sensor development, uneven background luminescence and low initial fluorescence reduce the quality of the images, potentially leading to the segmentation errors, such as the missing cells or drawing an intact ROI for multiple touching cells. We minimize these effects by pre-processing the image data using the rolling-ball algorithm to remove the background noise. Since the number of cells for fluorescent imaging is usually above 50, and the field of view is empirically chosen , missing a few cells barely causes significant effect to the overall time-lapsed evaluation of the sensor.

Further investigation on the performance of new segmentation methods needs to be done. In a recently published study on the segmentation and tracking of human dendritic cells, Braiki *et al.* uses the k-means clustering method to compute the segmentation result in the first frame of a time-lapsed imaging of dendritic cells and track the cells using the active contours with the first segmentation result as the *a priori* knowledge [60]. This approach demonstrates high segmentation and tracking accuracy while having a much lower computational complexity compared to the deep-learning methods. It is necessary to follow the new trend in this field in order to optimize our image analysis pipeline.

5.2.2 Single-Cell Tracking

COINN is able to identify the cells that present from the first to last frame and correct their labels to maintain the temporal correspondence through the frames. The results of single-cell tracking shows the portion of cells that demonstrate less than 1% fluorescent change upon agonist administration varies from trial to trial. Removing these cells from the data increases the overall fluorescent output as well as the variance. This result verifies the difference in fluorescent response of the cardiomyocytes derived from the same hiPSC population and also brings awareness to the effect of cell-to-cell difference in evaluating the sensor performance.

We acknowledge the existence of cell-to-cell variance in all experimental environments, thus the purpose of visualizing the fluorescent response of the individual cells is to raise a question on whether all cells from the field of view should be used to show the sensor performance, or only the responsive ones reflect the true fluorescent change induced by the agonist. Because the experimental procedures of sensor screening are both time-consuming and labor-intensive, optimizing the information extracted from every single image is a critical aspect to improve the entire pipeline of sensor development. Furthermore, the results from single-cell analysis reveal the significant effect of low-response cells. Future work on understanding the causes behind the low-response cells should be conducted.

Quantitative examination of COINN performance needs to be conducted. We verify the accuracy of COINN in CPA-treated cardiomyocytes by randomly select 5 cells from the output data and visually examine their labels and positions through the entire course of imaging. Due to the intensive labor, this approach only works with the images of less than 50 frames. As documented in many cell segmentation and tracking studies, there are tasks and solutions annotated by the experts to examine the performance of algorithms in these two fields [4, 48, 53]. Verification on the accuracy of the combined Cellpose segmentation and COINN single-cell tracking can provide evidence to the single-cell analysis.

Most of the single-cell tracking analysis results are based on the imaging from hiPSC-derived cardiomyocytes upon CPA administration because of the moderate number of cells in the field of view ($n \approx 60$). We use six trials of purified hiPSC-derived cardiomyocytes treated with the same CPA concentration. The mechanism of cardiomyocytes can be different from that of the other types of cells. Future study will focus on verifying the single-cell tracking results in different types of cells transfected with various H_2O_2 sensors, quantifying the existence of the low-response cells upon agonist administration.

One limitation of the single-cell tracking method proposed in this thesis is that it removes the cells with missing temporal correspondence, or so-called ”sporadic cells”. For the scope of this thesis, these cells are only excluded from the single-cell tracking result and analysis, and their fluorescent readout is still used for the result of sensor characterization. Removing the sporadic cells from the overall data slightly smooths the generated curve of fluorescent readout and increases the overall intensity of both the control and CPA-treated groups (Figure.A.4). Because the accuracy of this tracking method highly depends on the performance of Cellpose segmentation, improving the segmentation accuracy of Cellpose can reduce the number of sporadic cells. The visual inspection of these sporadic cell also suggest low initial fluorescence of these cells. Further investigation to quantitatively examine the mechanisms behind the sporadic cells needs to be conducted.

5.2.3 Volumetric Control

The volumetric design of HRM63-mCherry corrects some of the problems occurred in the original intensiometric sensors, such as the change in protein expression. Recording both the intensity from mCherry and cpGFP at each frame is a simple method that enables pixel-wise ratiometric reading. Combining the use of single-cell tracking and volumetric control, we use a new approach to represent the fluorescent change while accounting for the cell-to-cell difference as well as the effect of aggregation, minimizing the potential biological factors that interfere with the reflection of oxidation level.

The mCherry fused to the non-flexible region on the sensing domain serves as the control in the ratiometric reading, but introducing double amount of fluorescent proteins to cells may increase the occasion of aggregation, especially when the sensor are tranfected to smaller cells. We thus adjust the experimental and computational protocol to accommodate this change. The top and bottom cutoff values of the protein expression level represented by the F_{610} intensity are determined empirically to 10% and 35%. This value can be further tuned to optimize the aggregation removal.

5.2.4 Machine Learning-Based Classification

Though the mechanism behind the responsiveness of sensor-transfected cells to the administrated agonist remains unknown, we aim to explore the potential factors that determine the cell responsiveness to agonist administration from the computational perspective. Machine learning-based supervised classification has been applied to many studies on the variability in cell and tissue morphology [82], but the trained classifiers using the provided seven image features in this thesis only demonstrate moderate prediction accuracy. The result suggests that the SVM model using RBF kernel trained with y-position of the cell centroid is a potential direction to proceed. Additionally, the prediction accuracy of time-dependent one-feature classification is higher than that of the time-independent all-feature classification. It shows that the temporal pattern of the features is an important criteria for the classifiers to determine cell responsiveness.

For the scope of this thesis, all image features are one-dimensional data, which may limit the performance of the classifier. Moreover, the seven features used in this analysis are mostly on the position and shape of the cell, lacking the description on the cell textures. Orlov `et al.` proposed more complex features in a study of multi-purpose image classification, which requires the wavelet transformation of the given grey-scale cell image [83]. Thus, future study will focus on using such features in the classification, investigating the features that are responsible to the cell responsiveness.

The dataset used to train the classifiers can be expanded in the future study. We used the data from six trials of sensor-transfected hiPSC-derived cardiomyocytes to train and test the classifers, so the results can be specific to this particular cell types. Shifat-E-Rabbi *et al.* uses five datasets of different cell types to discriminate the cells [45]. A similar strategy will be used in the future work to test the generality of the result.

Chapter 6

CONCLUSION

Among all the analytical tools for intracellular monitoring of molecules, GEFI opens the possibility for quantifiable ROS detection because of its high temporal resolution, subcellular sensitivity and cellular type specificity. Various designs on GEFIs specifically detecting H_2O_2 have been proposed in recent year [8, 9, 10, 11, 12, 13, 14, 41], but the sensor sensitivity in H_2O_2 lower than 50 μM is often a challenge [8, 9, 10, 11], or using yeast as a sensor generation platform raises concerns on its application in mammalian cells [13, 14]. HRM63 serves as the first variant that uses cpGFP as the reporter while demonstrating high sensitivity and brightness upon 10 μM H_2O_2 stimulation, enabling the H_2O_2 detection in the physiological condition.

For the computational evaluation, we first show the application of Cellpose, an outperforming generalist segmentation method, in extracting image properties during H_2O_2 sensor development. Based on the nearest-neighbor theory and segmentation result from Cellpose, we also develop a single-cell tracking method named COINN to analyze the cell-to-cell difference upon agonist administration during the fluorescent imaging of HRM63-transfected cells. We then show that using the pixel-wise ratiometric reading of HRM63-mCherry reduces the variance among the data variance. Removing the cells that have extreme protein expression level also improves the separation of conditioned data from the control. Combining both the volumetric reading and single-cell tracking, we train the machine learning-based classifiers to identify the correlation between the image features and cell response to agonist administration. Although we did not identify a dominant feature, the SVM classifier using the time-dependent y-position of cell centroid demonstrates its potential application in predicting the cell responsiveness.

As in many other researches in the field of protein, protein sensor design and development is like working in a black box. Cells from the same population can demonstrate distinct cellular activities, hindering the production of the reproducible results. Though we are able to present HRM63 as an effective sensor detecting the H_2O_2 production in various cellular mechanisms, the biology behind many phenomenon regarding sensor dynamic still remains unknown. Thus, we combine the experimental and computational evaluations to explore the details of the relevant mechanisms, depicting the story of HRM63 from a new perspective. These tests have important impact on the pipeline of developing genetically transfected sensors, facilitating the relative researches involving ROS-mediated mechanisms.

BIBLIOGRAPHY

[1] J. N. Moloney and T. G. Cotter, “Ros signalling in the biology of cancer,” *Seminars in Cell and Developmental Biology*, vol. 80, 2018.

[2] S. S. Schattauer, B. B. Land, K. L. Reichard, A. D. Abraham, L. M. Burgeno, J. R. Kuhar, P. E. M. Phillips, S. E. Ong, and C. Chavkin, “Peroxiredoxin 6 mediates gαi protein-coupled receptor inactivation by cjun kinase,” *Nature communications*, vol. 8, no. 1, 2017.

[3] E. Ho, K. K. Galougahi, C.-C. Liu, R. Bhindi, and G. A. Figtree, “Biological markers of oxidative stress: Applications to cardiovascular research and practice,” *Redox Biol*, vol. 1, no. 1, 2013.

[4] C. Stringer, T. Wang, M. Michaelos, and M. Pachitariu, “Cellpose: a generalist algorithm for cellular segmentation,” *Nature Methods*, vol. 18, 2021.

[5] G. Loor, J. Kondapalli, J. M. Schriewer, N. S. Chandel, T. L. V. Hoek, and P. T. Schumacker, “Menadione triggers cell death through ros-dependent mechanisms involving parp activation without requiring apoptosis,” *Free Radic Biol Med*, vol. 49, no. 12, 2010.

[6] A. A. Starkov, A. Y. Andreyev, S. F. Zhang, N. N. Starkova, M. Korneeva, M. Syromyatnikov, and V. N. Popov, “Scavenging of h2o2 by mouse brain mitochondria,” *J Bioenerg Biomembr*, vol. 46, no. 6, 2014.

[7] M. P. Rigobello, A. Folda, M. C. Baldoin, G. Scutari, and A. Bindoli, “Effect of auranofin on the mitochondrial generation of hydrogen peroxide. role of thioredoxin reductase,” *Free Radical Research*, vol. 39, no. 7, 2005.

[8] V. V. Belousov, A. F. Fradkov, K. A. Lukyanov, D. B. Staroverov, K. S. Shakhbazov, A. V. Terskikh, and S. Lukyanov, “Genetically encoded fluorescent indicator for intracellular hydrogen peroxide,” *Nature Methods*, vol. 3, 2006.

[9] K. N. Markvicheva, D. S. Bilan, N. M. Mishina, A. Y. Gorokhovatsky, L. M. Vinokurov, S. Lukyanov, and V. V. Belousov, “A genetically encoded sensor for h2o2 with expanded dynamic range,” *Bioorg Med Chem*, vol. 19, no. 3, 2011.

[10] D. S. Bilan, L. Pase, L. Joosen, A. Y. Gorokhovatsky, Y. G. Ermakova, T. W. J. Gadella, C. Grabher, C. Schultz, S. Lukyanov, and V. V. Belousov, "Hyper-3: a genetically encoded h(2)o(2) probe with improved performance for ratiometric and fluorescence lifetime imaging," *ACS Chem Biol*, vol. 8, no. 3, 2013.

[11] Y. G. Ermakova, D. S. Bilan, M. E. Matlashov, N. M. Mishina, K. N. Markvicheva, O. M. Subach, F. V. Subach, I. Bogeski, M. Hoth, G. Enikolopov, and V. V. Belousov, "Red fluorescent genetically encoded indicator for intracellular hydrogen peroxide," *Nature Communications*, vol. 5, no. 5222, 2014.

[12] V. V. Pak, D. Ezerin, O. G. Lyublinskaya, S. Vriz, J. Messens, and V. V. Belousov, "Ultrasensitive genetically encoded indicator for hydrogen peroxide identifies roles for the oxidant in cell migration and mitochondrial function," *Cell Metabolism*, vol. 31, 2020.

[13] M. Gutscher, M. C. Sobotta, G. H. Wabnitz, S. Ballikaya, A. J. Meyer, Y. Samstag, and T. P. Dick, "Proximity-based protein thiol oxidation by h2o2-scavenging peroxidases," *J Biol Chem*, vol. 284, no. 46, 2009.

[14] B. Morgan, K. V. Laer, T. N. E. Owusu, D. Ezeriņa, D. Pastor-Flores, P. S. Amponsah, A. Tursch, and T. P. Dick, "Real-time monitoring of basal h2o2 levels with peroxiredoxin-based probes," *Nat Chem Biol*, vol. 12, no. 6, 2016.

[15] K. Brieger, S. Schiavone, F. J. M. Jr., and K.-H. Krause, "Reactive oxygen species: from health to disease," *Swiss Med Wkly*, vol. 142, 2012.

[16] W. Ahmad, B. Ijaz, K. Shabbiri, F. Ahmed, and S. Rehman, "Oxidative toxicity in diabetes and alzheimer's disease: mechanisms behind ros/ rns generation.," *Journal of biomedical science*, vol. 24, no. 1.

[17] R. R. Bartz, H. B. Suliman, and C. A. Piantadosi, "Redox mechanisms of cardiomyocyte mitochondrial protection.," *Front Physiol*, vol. 6, no. 291, 2015.

[18] J. R. Stone and S. Yang, "Hydrogen peroxide: a signaling messenger.," *Antioxid Redox Signal.*, vol. 8, no. 34, 2006.

[19] A. W. Mehendale, M. P. Goldman, and R. P. Mehendale, "Opioid overuse pain syndrome (oops): the story of opioids prometheus unbound.," *J Opioid Manag*, vol. 9, no. 6, pp. 421–38, 2013.

[20] S. Scholl, P. Seth, M. Kariisa, N. Wilson, and G. Baldwin, "Drug and opioid-involved overdose deaths — united states, 2013–2017," *MMWR Morb Mortal Wkly Rep*, vol. 67, 2019.

[21] S. A. Ryan, “Calculating the real costs of the opioid crisis,” *Pediatrics*, vol. 141, no. 4.

[22] S. P. Loukogeorgakis, M. J. van den Berg, R. Sofat, D. Nitsch, M. Charakida, B. Haiyee, E. de Groot, R. J. MacAllister, T. W. Kuijpers, and J. E. Deanfield, “Role of nadph oxidase in endothelial ischemia/reperfusion injury in humans,” *Circulation*, vol. 121, no. 21, 2010.

[23] K. E. Wyche, S. S. Wang, S. I. D. Kathy K. Griendling, H. Austin, S. Rao, B. Fink, D. G. Harrison, and A. M. Zafari, “C242t cyba polymorphism of the nadph oxidase is associated with reduced respiratory burst in human neutrophils,” *Hypertension*, vol. 43, no. 6, 2004.

[24] T. Akaike, N. Du, G. Lu, S. Minamisawa, Y. Wang, and H. Ruan, “A sarcoplasmic reticulum localized protein phosphatase regulates phospholamban phosphorylation and promotes ischemia reperfusion injury in the heart,” *J Am Coll Cardiol Basic Trans Science*, vol. 2, no. 2, 2017.

[25] “Heart disease facts.” `https://www.cdc.gov/heartdisease/facts.htm`. (accessed: 04.03.2021).

[26] K. H. Fisher-Wellman, T. A. Mattox, K. Thayne, L. A. Katunga, J. D. L. Favor, P. D. Neufer, R. C. Hickner, C. J. Wingard, and E. J. Anderson, “Novel role for thioredoxin reductase-2 in mitochondrial redox adaptations to obesogenic diet and exercise in heart and skeletal muscle.,” *J Physiol.*, vol. 591, no. 14, 2013.

[27] H. Dana, Y. Sun, B. Mohar, B. K. Hulse, A. M. Kerlin, J. P. Hasseman, G. Tsegaye, A. Tsang, A. Wong, R. Patel, J. J. Macklin, Y. Chen, A. Konnerth, V. Jayaraman, L. L. Looger, E. R. Schreiter, and K. S. amd Douglas S. Kim, “High-performance calcium sensors for imaging activity in neuronal populations and microcompartments,” *Nature Methods*, vol. 16, 2019.

[28] F. St-Pierre, J. D. Marshall, Y. Yang, Y. Gong, M. J. Schnitzer, and M. Z. Lin, “High-fidelity optical reporting of neuronal electrical activity with an ultrafast fluorescent voltage sensor,” *Nature Neuroscience*, vol. 17, 2014.

[29] I. Jo, I.-Y. Chung, H.-W. Bae, J.-S. Kim, S. Song, Y.-H. Cho, , and N.-C. Ha, “Structural details of the oxyr peroxide-sensing mechanism,” *PNAS*, vol. 112, no. 20, 2015.

[30] B. Li, R. Shahid, P. Peshkepija, and M. Zimmer, “Water diffusion in and out of the β-barrel of gfp and the fast maturing fluorescent protein, turbogfp,” *Chem Phys*, vol. 392, no. 1, 2012.

[31] L. Yang, S. Nian, G. Zhang, E. Sharman, H. Miao, X. Zhang, and X. Chen, “Role of hydrogen bonding in green fluorescent protein-like chromophore emission,” *Scientific Reports*, vol. 9, no. 11640, 2019.

[32] A. I. Kostyuk, A. S. Panova, A. D. Kokova, D. A. Kotova, D. I. Maltsev, O. V. Podgorny, V. V. Belousov, and D. S. Bilan, "In vivo imaging with genetically encoded redox biosensors," *Int J Mol Sci*, vol. 21, no. 21, 2020.

[33] R. J. Bevan, M. F. Durand, P. T. Hickenbotham, G. D. Kitas, P. R. Patel, H. R. G. Ian D Podmore, H. L. Waller, and J. Lunec, "Validation of a novel elisa for measurement of mda-ldl in human plasma," *Free Radic Biol Med*, vol. 35, no. 5, 2003.

[34] G. Ozansoy, B. Akin, F. Aktan, and C. Karasu, "Short-term gemfibrozil treatment reverses lipid profile and peroxidation but does not alter blood glucose and tissue antioxidant enzymes in chronically diabetic rats," *Mol Cell Biochem*, vol. 216, no. 1-2, 2001.

[35] S. Singh, S. Vrishni, B. K. Singh, I. Rahman, and P. Kakkar, "Nrf2-are stress response mechanism: a control point in oxidative stress-mediated dysfunctions and chronic inflammatory diseases," *Free Radic Res*, vol. 44, no. 11, 2010.

[36] D. Johnson, E. Allman, and K. Nehrke, "Regulation of acid-base transporters by reactive oxygen species following mitochondrial fragmentation," *Am J Physiol Cell Physiol*, vol. 302, no. 7, 2012.

[37] N. Kaludercic, S. Deshwal, and F. D. Lisa, "Reactive oxygen species and redox compartmentalization," *Front Physiol*, vol. 5, no. 285, 2014.

[38] Z. Liu, A. M. Celotto, G. Romero, P. Wipf, and M. J. Palladino, "Genetically encoded redox sensor identifies the role of ros in degenerative and mitochondrial disease pathogenesis," *Neurobiol Dis*, vol. 45, no. 1, 2012.

[39] G. T. Hanson, R. Aggeler, D. Oglesbee, M. Cannon, R. A. Capaldi, R. Y. Tsien, and S. J. Remington, "Investigating mitochondrial redox potential with redox-sensitive green fluorescent protein indicators," *J Biol Chem*, vol. 279, no. 13, 2004.

[40] Y. P. Hung, J. G. Albeck, M. Tantama, and G. Yellen, "Imaging cytosolic nadh-nad+ redox state with a genetically encoded fluorescent biosensor," *Cell Metab*, vol. 14, no. 4, 2011.

[41] E. P. Melo, C. Lopes, P. Gollwitzer, S. Lortz, S. Lenzen, I. Mehmeti, C. F. Kaminski, D. Ron, and E. Avezov, "Triper, an optical probe tuned to the endoplasmic reticulum tracks changes in luminal h2o2," *BMC Biol*, vol. 15, no. 24, 2017.

[42] S. Fourquet, M.-E. Huang, B. D'Autreaux, and M. B. Toledano, "The dual functions of thiol-based peroxidases in h2o2 scavenging and signaling," *Antioxid Redox Signal*, vol. 10, no. 9, 2008.

[43] M. B. Elowitz, A. J. Levine, E. D. Siggia, and P. S. Swain, “Stochastic gene expression in a single cell,” *Science*, vol. 297, no. 5584, 2002.

[44] M. Radzinski, R. Fassler, O. Yogev, W. Breuer, N. Shai, J. Gutin, S. Ilyas, Y. Geffen, S. Tsytkin-Kirschenzweig, Y. Nahmias, T. Ravid, N. Friedman, M. Schuldiner, and D. Reichmann, “Temporal profiling of redox-dependent heterogeneity in single cells,” *eLife*, vol. 7, 2018.

[45] M. Shifat-E-Rabbi, X. Yin, C. E. Fitzgerald, and G. K. Rohde, “Cell image classification: a comparative overview,” *Cytometry Part A*, 2020.

[46] C. A. Schneider, W. S. Rasband, and K. W. Eliceir, “Nih image to imagej: 25 years of image analysis,” *Nature Methods*, vol. 9, 2012.

[47] I. F. Sbalzarini, “Seeing is believing: Quantifying is convincing: Computational image analysis in biology,” *Adv Anat Embryol Cell Biol*, vol. 219, 2016.

[48] V. Ulman, M. Maška, K. E. G. Magnusson, O. Ronneberger, C. Haubold, N. Harder, P. Matula, P. Matula, D. Svoboda, M. Radojevic, I. Smal, K. Rohr, J. Jaldén, H. M. Blau, O. Dzyubachyk, B. Lelieveldt, P. Xiao, Y. Li, S.-Y. Cho, A. C. Dufour, J.-C. Olivo-Marin, C. C. Reyes-Aldasoro, J. A. Solis-Lemus, R. Bensch, T. Brox, J. Stegmaier, R. Mikut, S. Wolf, F. A. Hamprecht, T. Esteves, P. Quelhas, Ömer Demirel, L. Malmström, F. Jug, P. Tomancak, E. Meijering, A. Muñoz-Barrutia, M. Kozubek, and C. O. de Solorzano, “An objective comparison of cell tracking algorithms,” *Nat Methods*, vol. 14, no. 12, 2017.

[49] J. F. Dorn, G. Danuser, , and G. Yang, “Computational processing and analysis of dynamic fluorescence image data,” *Methods in Cell Biology*, vol. 85, 2008.

[50] S. Beucher and F. Meyer, “The morphological approach to segmentation: The watershed transformation,” *Mathematical morphology in image processing 34*, 1993.

[51] M. Gamarra, E. Zurek, H. J. Escalante, L. Hurtado, and H. San-Juan-Vergara, “Split and merge watershed: a two-step method for cell segmentation in fluorescence microscopy images,” *Biomed Signal Process Control*, vol. 53, 2019.

[52] P. Duan, W. Cheng, Q. Qian, Q. Zhang, R. Yang, and Y. Pan, “Overlapping cervical cell image segmentation based on bottleneck detection and watershed algorithm,” *Zhongguo Yi Liao Qi Xie Za Zhi*, vol. 44, no. 1, 2020.

[53] O. Ronneberger, P.Fischer, and T. Brox, “U-net: Convolutional networks for biomedical image segmentation,” in *Medical Image Computing and Computer-Assisted Intervention (MICCAI)*, vol. 9351 of *LNCS*, pp. 234–241, Springer, 2015. (available on arXiv:1505.04597 [cs.CV]).

[54] A. Dufour, V. Shinin, S. Tajbakhsh, N. Guillén-Aghion, J.-C. Olivo-Marin, and C. Zimmer, "Segmenting and tracking fluorescent cells in dynamic 3-d microscopy with coupled active surfaces," *IEEE Transactions on Medical Imaging*, vol. 14, no. 9, 2005.

[55] O. Dzyubachyk, W. A. van Cappellen, J. Essers, W. J. Niessen, S. Member, and E. Meijering, "Advanced level-set-based cell tracking in time-lapse fluorescence microscopy," *IEEE Transactions on Medical Imaging*, vol. 29, no. 3, 2010.

[56] M. Maska, O. Danek, S. Garasa, A. Rouzaut, A. Munoz-Barrutia, and C. O. de Solorzano, "Segmentation and shape tracking of whole fluorescent cells based on the chan–vese model," *IEEE Transactions on Medical Imaging*, vol. 32, no. 6, 2013.

[57] O. Al-Kofahi, R. J. Radke, S. K. Goderie, Q. Shen, S. Temple, and B. Roysam, "Automated cell lineage construction: a rapid method to analyze clonal development established with murine neural progenitor cells," *Cell Cycle*, vol. 5, no. 3, 2006.

[58] F. Boukari and S. Makrogiannis, "Automated cell tracking using motion prediction-based matching and event handling," *IEEE/ACM Trans Comput Biol Bioinform*, vol. 17, no. 3, 2020.

[59] J. Jara-Wilde, I. Castro, C. G. Lemus, K. Palma, F. Valdés, V. Castañeda, N. Hitschfeld, M. L. Concha, and S. Härtel, "Optimising adjacent membrane segmentation and parameterisation in multicellular aggregates by piecewise active contours," *J Microsc*, vol. 278, no. 2, 2020.

[60] M. Braiki, A. Benzinou, K. Nasreddine, and N. Hymery, "Automatic human dendritic cells segmentation using k-means clustering and chan-vese active contour model," *Computer Methods and Programs in Biomedicine*, vol. 195, 2020.

[61] E. Meijering, I. Smal, and G. Danuser, "Tracking in molecular bioimaging," *IEEE Signal Processing Magazine*, vol. 46, 2006.

[62] O. Al-Kofahi, R. J. Radke, S. K. Goderie, Q. Shen, S. Temple, and B. Roysam, "Automated cell lineage construction: A rapid method to analyze clonal development established with murine neural progenitor cells," *Cell Cycle*, vol. 5, no. 3.

[63] A. Ponti, A. Matov, M. Adams, S.Gupton, C.M.Waterman-Storer, and G.Danuser, "Periodic patterns of actin turnover in lamellipodia and lamellae of migrating epithelial cells analyzed by quantitative fluorescent speckle microscopy," *Biophysical Journal*, vol. 89, no. 5, 2005.

[64] N. A. Hamilton, R. S. Pantelic, K. Hanson, and R. D. Teasdale, "Fast automated cell phenotype image classification," *BMC Bioinformatics*, vol. 8, no. 110, 2007.

[65] R. F. Murphy, M. V. Boland, and M. Velliste, “Towards a systematics for protein subcelluar location: quantitative description of protein localization patterns and automated analysis of fluorescence microscope images,” *Proc Int Conf Intell Syst Mol Biol*, vol. 8, 2000.

[66] J. C. Klima, L. A. Doyle, J. D. Lee, M. Rappleye, L. A. Gagnon, M. Y. Lee, E. P. Barros, A. A. Vorobieva, J. Dou, S. Bremner, J. S. Quon, C. M. Chow, L. Carter, D. L. Mack, R. E. Amaro, J. C. Vaughan, A. Berndt, B. L. Stoddard, and D. Baker, “Incorporation of sensing modalities into de novo designed fluorescence-activating proteins,” *Nat Commun*, vol. 12, no. 1, 2021.

[67] “Metamorph microscopy automation and image analysis software (rrid:scr_002368).” `http://www.moleculardevices.com/Products/Software/Meta-Imaging-Series/MetaMorph.html`. Accessed March 12, 2021.

[68] “Hydrogen peroxide, sds no. 008003009, sigma-aldrich corporation: Americas.” `https://www.sigmaaldrich.com/MSDS/MSDS/DisplayMSDSPage.do?country=US&language=en&productNumber=H1009&brand=SIGMA`. Accessed Jan 20, 2020.

[69] H. S. Kazuho Abe, “Menadione toxicity in cultured rat cortical astrocytes,” vol. 72, no. 4, 1996.

[70] X. Liu, L. Wang, J. Cai, K. Liu, M. Liu, H. Wang, and H. Zhang, “N-acetylcysteine alleviates h2o2-induced damage via regulating the redox status of intracellular antioxidants in h9c2 cells,” *Int J Mol Med*, vol. 43, no. 1, 2019.

[71] S. R. Sternberg, “Biomedical image processing,” *Computer*, vol. 16, no. 1, 1983.

[72] “Rolling ball background subtraction.” `https://imagej.net/Rolling_Ball_Background_Subtraction`. Accessed May 14, 2021.

[73] S. Daniels and C. J.Duncan, “Interaction of h2o2 and dithiothreitol and the genesis of cellular damage in the perfused rat heart,” *Comp Biochem Physiol C Comp Pharmacol Toxicol*, vol. 104, no. 1, 1993.

[74] H.-J. Choi, S.-J. Kim, P. Mukhopadhyay, S. Cho, J.-R. Woo, G. Storz, and S.-E. Ryu, “Structural basis of the redox switch in the oxyr transcription factor,” *Cell*, vol. 105, 2001.

[75] “Dtt (dithiothreitol).” `https://www.thermofisher.cn/order/catalog/product/R0861#/R0861`. Accessed May 12, 2021.

[76] T.-W. Chen, T. J. Wardill, . S. R. P. Yi Sun, S. L. Renninger, A. Baohan, E. R. Schreiter, R. A. Kerr, M. B. Orger, V. Jayaraman, L. L. Looger, K. Svoboda, and D. S. Kim, "Ultra-sensitive fluorescent proteins for imaging neuronal activity," *Nature*, vol. 499, no. 7458, 2013.

[77] G. Li, T. Liu, J. Nie, L. Guo, J. Chen, J. Zhu, W. Xia, A. Mara, S. Holley, and S. Wong, "Segmentation of touching cell nuclei using gradient flow tracking," *J Microsc*, vol. 231, 2008.

[78] M. Stefani and C. M. Dobson, "Protein aggregation and aggregate toxicity: new insights into protein folding, misfolding diseases and biological evolution," *Journal of Molecular Medicine*, vol. 81, 2003.

[79] J. Krasowska, M. Olasek, A. Bzowska, P. L. Clark, and B. Wielgus-Kutrowska, "The comparison of aggregation and folding of enhanced green fluorescent protein (egfp) by spectroscopic studies," *Spectroscopy*, vol. 24, 2010.

[80] M. M. Karasev, O. V. Stepanenko, K. A. Rumyantsev, K. K. Turoverov, and V. V. Verkhusha, "Near-infrared fluorescent proteins and their applications," *Biochemistry (Mosc)*, vol. 84, no. 1, 2019.

[81] D. M. Shcherbakova, M. Baloban, and V. V. Verkhusha, "Near-infrared fluorescent proteins engineered from bacterial phytochromes," *Curr Opin Chem Biol*, vol. 27, 2015.

[82] A. Kan, "Machine learning applications in cell image analysis," *Immunology and Cell Biology*, vol. 95, no. 6, 2017.

[83] N. Orlov, L. Shamir, T. Macura, J. Johnston, M. Eckley, and I. G. Goldberg, "Wnd-charm: Multi-purpose image classification using compound image transforms," *Pattern Recognit Lett*, vol. 29, no. 11, 2008.

Appendix A

ADDITIONAL FIGURES AND TABLES

This page is intentionally left blank for formatting purposes.

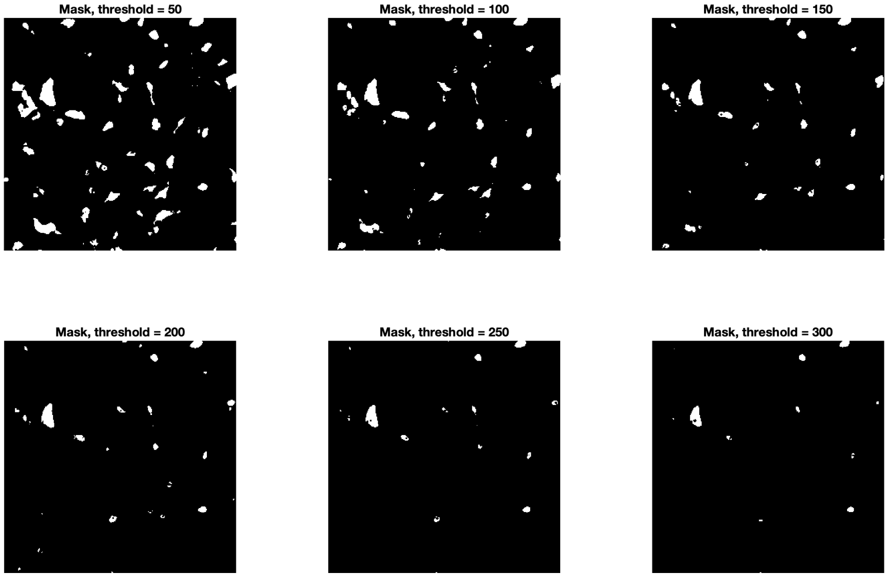

Figure A.1: **Simple thresholding segmentation method demonstration.** Image data is the first frame of the time-lapse hiPSC-derived cardiomyocytes transfected with HRM63-mCherry variant stimulated with cyclopiazonic acid (CPA). The trade-offs between the touching-cell separation and the number of detecting ROIs make the thresholding method no longer desirable.

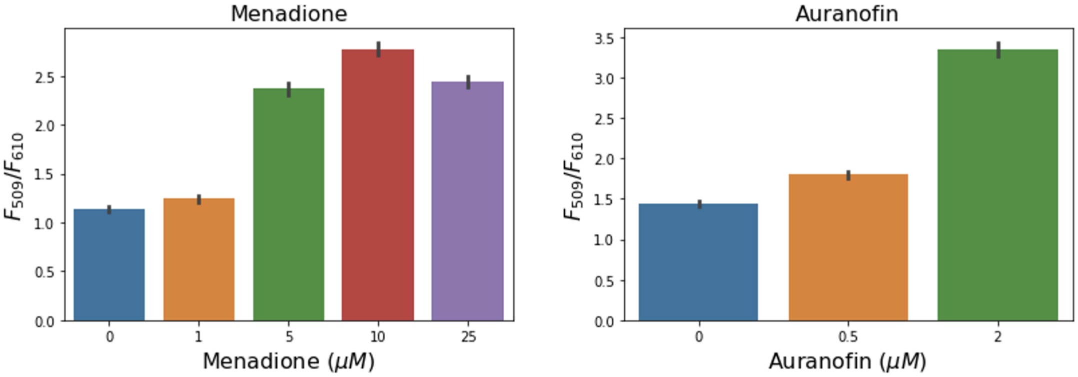

Figure A.2: **HRM63-mCherry variant demonstrates distinct performance stimulated with concentration gradient of menadione and auranofin in HEK293 cells.** Both menadione and auranofin induce intracellular H_2O_2 production [5, 6, 7].

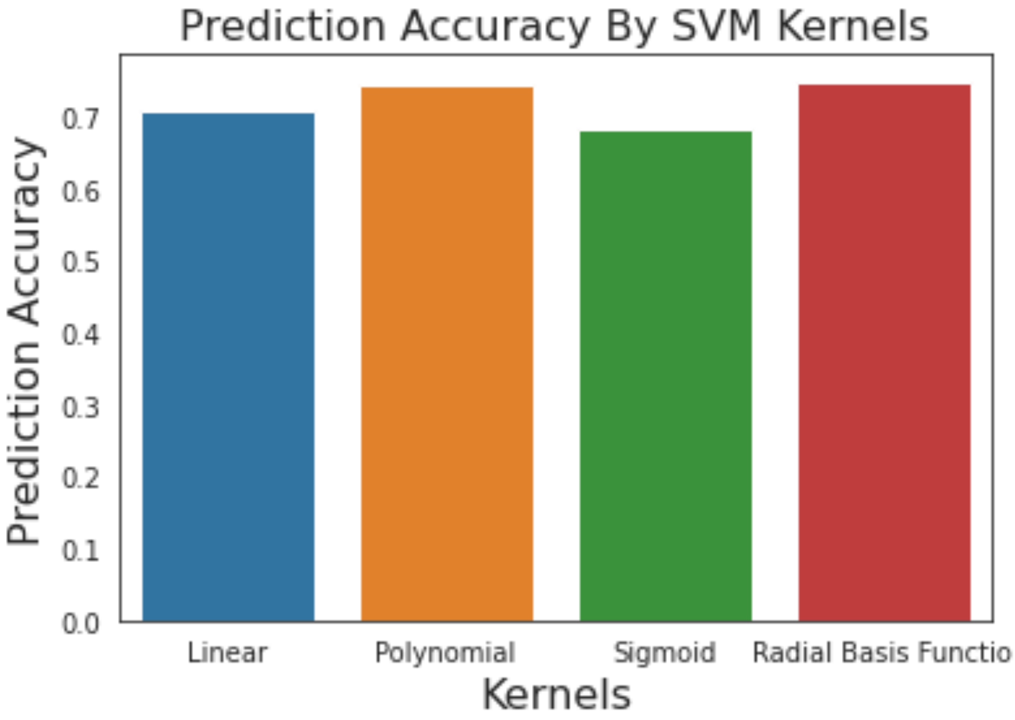

Figure A.3: **Comparison of the average prediction Accuracy using different support vector machine kernels in the classification of whether HRM63-mCherry-transfected cardiomyocytes respond to CPA administration.** The default radial basis function kernel demonstrates the highest prediction accuracy. Seven image features are used to compute the average prediction accuracy of each kernel.

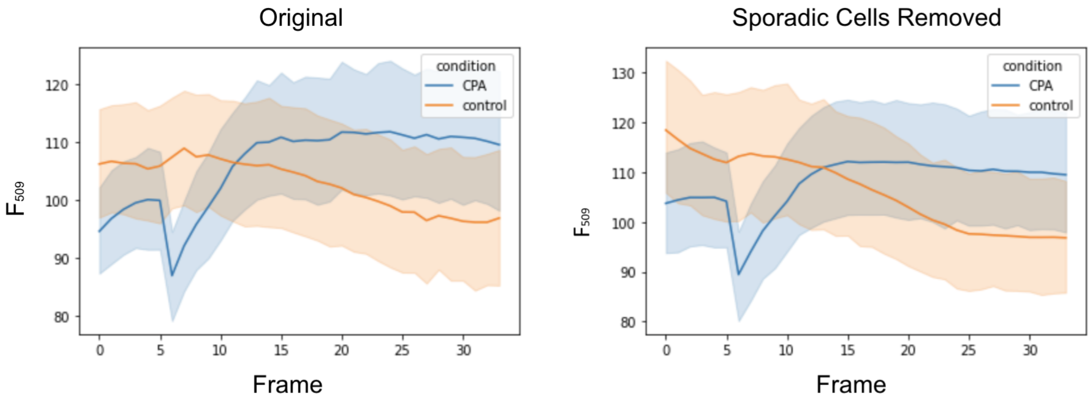

Figure A.4: **Removal of sporadic cells slightly smooths the curve of fluorescent output and increases the mean F_{509} intensity of both the control and CPA-treated group.** The sporadic cells are mostly due to the Cellpose segmentation error in detecting cells with low signal-to-noise ratio.

Name	**Sensing Domain**	**Platform**	**Strain**	**Excitation Wavelength**	**Reporter Domain**	**Emission Wavelength**	**Reported *in vitro* Fold Change at Saturation**	**pH Stable**
HyPer	OxyR-RD	Bacteria	E. coli	420nm/500nm	cpYFP	516nm	3.3 (250nM in purified protein)	No
HyPer2	OxyR-RD	Bacteria	E. coli	420nm/500nm	cpYFP	516nm	5.5 (150 uM in Hela cells)	No
HyPer3	OxyR-RD	Bacteria	E. coli	420nm/500nm	cpYFP	516nm	6 (150 uM in Hela cells)	No
HyPerRed	OxyR-RD	Bacteria	E. coli	570nm	cpmApple	620nm	2 (300 uM in purified protein)	No
HyPer7	OxyR-RD	Bacteria	N. meningitidis	400nm/499nm	cpYFP	516nm	3.5 (2uM in purified protein)	Yes
roGFP2-Orp1	Orp1	Yeast	S. cerevisiae	400nm/499nm	roGFP2	511nm	6 (1000 uM in purified protein)	Yes
roGFP2-Tsa2	Tsa2	Yease	S. cerevisiae	400nm/499nm	roGFP2	511nm	2 (1000 uM in purified protein)	Yes

Table A.1: **Summary of genetically encoded fluorescent sensors detecting** H_2O_2 **[8, 9, 10, 11, 12, 13, 14].** The pH stability of sensors only refer to the physiological pH ranging from 6 to 8 [12]

	Logistic Regression	Decision Tree	K-Nearest Neighbors	Linear Discriminant Analysis	Support Vector Machine	**Average**
F_{610}	0.714	0.536	0.691	0.709	0.741	0.678
Area (pixel)	0.595	0.623	0.659	0.618	0.718	0.643
Eccentricity	0.750	0.618	0.659	0.645	0.750	0.685
Major Axis Length	0.632	0.577	0.641	0.695	0.736	0.656
Orientation	0.727	0.509	0.655	0.709	0.745	0.669
X-Position	0.691	0.609	0.659	0.677	0.759	0.679
Y-Position	0.695	0.632	0.695	0.723	0.791	0.707
Average	0.686	0.586	0.666	0.682	0.749	0.674

Table A.2: **Prediction accuracy of the cell responsiveness to CPA administration in HRM63-mCherry-transfect hiPSC-derived cardiomyocytes using 5 different classification models.** The accuracy result is the average from 10 random training and testing group splitting. Seven image properties are selected to train the given models. The combination of y-position and support vector machine model produces the highest accuracy.

Appendix B

PYTHON CODE

Here is the link to the Google Colaboratory that contains the script of COINN and machine learning-based classification:

`https://colab.research.google.com/drive/1Xo1wigiCvlzwHNlEJPLKAsIJ-oxuyvp7?usp=sharing`